AIAA--2006-6948

"Fundamental" Parametric Geometry Representations for Aircraft Component Shapes

Brenda M. Kulfan and John E. Bussoletti
Boeing Commercial Airplane Group
Seattle, Washington

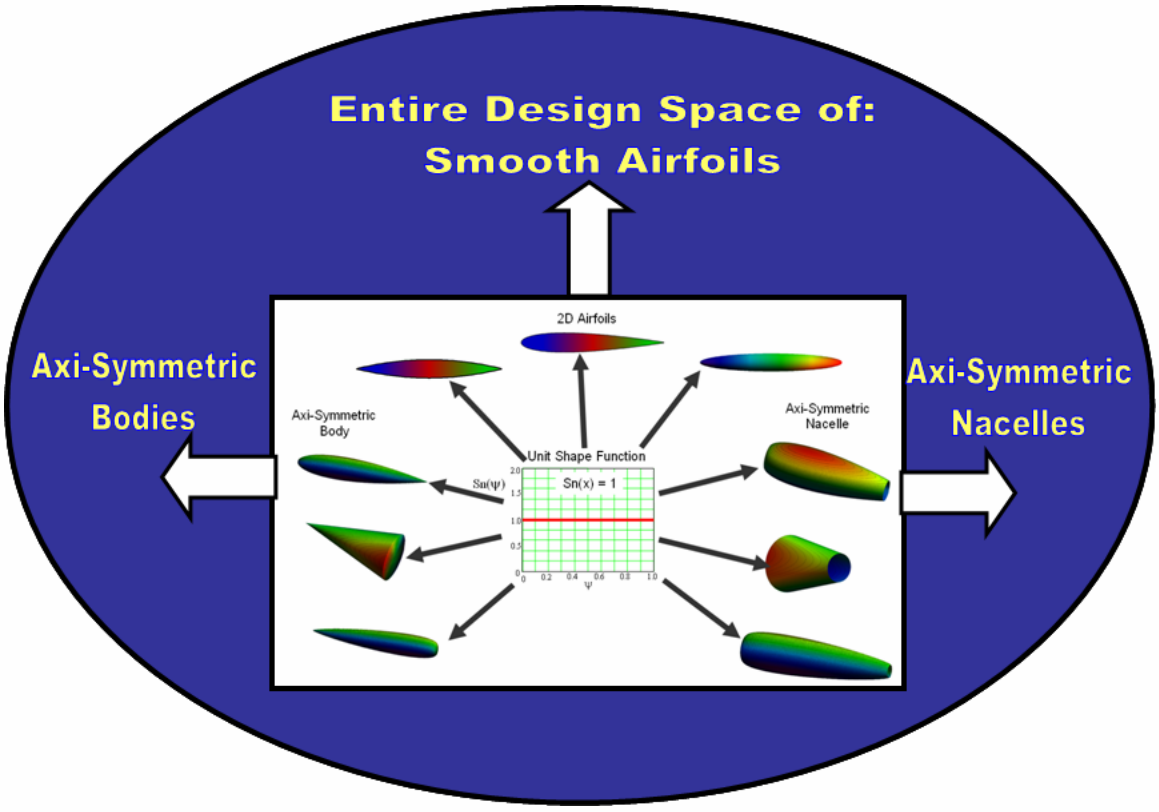

11th AIAA/ISSMO Multidisciplinary Analysis and Optimization Conference:
The Modeling and Simulation Frontier for Multidisciplinary Design Optimization
6 - 8 September 2006
Renaissance Portsmouth Hotel
Portsmouth, Virginia

"Fundamental" Parametric Geometry Representations for Aircraft Component Shapes

Brenda M. Kulfan* and John E. Bussoletti.†
Boeing Commercial Airplane Group, Seattle, Washington, 98124

The mathematical description of a nacelle, body or airfoil having a round nose and pointed aft-end is a continuous but non-analytic function because of the infinite slope at the nose and the corresponding large variations of curvature over the surface. Consequently, a large number of coordinates are typically required to describe the geometry. The general mathematical formulation necessary to describe an airfoil, axi-symmetric body or nacelle, is defined in order to develop a "fundamental" geometric transformation technique. This method includes the introduction of a simple analytic and well behaved "shape function" that describes the geometry. The "shape function" provides the ability to directly control key geometry parameters such as leading edge radius, trailing edge boattail angle, and closure to a specified aft thickness.

A "class function" is defined that generalizes the method for a wide variety of geometries. The "shape function" and "class function" methodology provides a unified approach for describing rather arbitrary 2D and 3D geometries. Examples of using this approach to produce a variety of 2D and 3D geometries are shown to illustrate the versatility of this new methodology.

I. Introduction

An aircraft configuration typically consists of two basic defining shapes[1] .

1. Class 1: Wing airfoil type shapes that define such components as:
   - Airfoils
   - Aircraft wings
   - helicopter rotors
   - turbomachinery blades
   - Horizontal and vertical tails, canards
   - Winglets
   - Pylons / struts
   - Nacelles (defined by streamwise profiles)
   - Bodies of Revolution

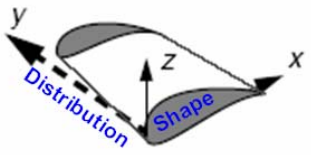

2. Class 2: Body cross-section type shapes that define such components as:
   - Aircraft fuselages (cross sections)
   - Rotor hubs and shrouds
   - Channels, ducts and tubing
   - Axisymmetric bodies
   - Lifting Bodies
   - Nacelles (when defined by cross sections)

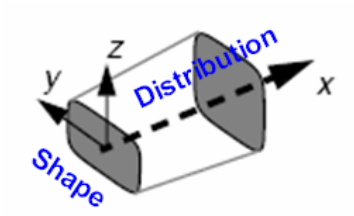

The distributions of these two fundamental shapes define each of the aircraft components. The particular features of the defining shapes are indeed quite dependent on the application as well as the flow environment especially the cruise Mach number (fig. 1). In some very highly integrated configurations such as hypersonic wave riders, the individual components may not be readily discernible. However the concepts presented in this paper will still apply.

Some components such as nacelles may be defined utilizing either of the two fundamental types. For example, a nacelle may be defined with airfoil type sections that are distributed circumferentially around the nacelle centerline. A nacelle could also be defined by body type cross-sections that are distributed along the axis of the nacelle.

In this paper we will initially focus on the class 1 type of airfoil shapes that have a round nose and a pointed aft-end. It will be shown that the methods developed to represent these airfoil geometries will apply equally well to other airfoil nose and aft-end shapes as well as to the class 2 types of body cross-section geometries.

---

* Engineer/Scientist – Technical Fellow, Enabling Technology & Research, PO Box 3707, Seattle, WA 98124 / MS 67-LF, AIAA Member
† Engineer/Scientist, Enabling Technology & Research, PO Box 3707, Seattle, WA 98124 / MS 67-LF

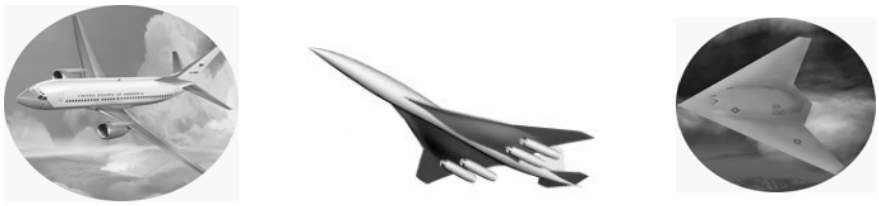

Figure 1. Fundamental Aerodynamic Configuration Defining Elements

II. Round Nose Airfoil Representation

Round nose airfoils have an infinite slope and an infinite 2nd derivative at the leading edge and large variations of curvature over the airfoil surface. A mathematical description of an airfoil must therefore deal with a rather complex non-analytic function over the surface of the airfoil. Consequently a large number of "X,Z" coordinates are typically required, along with a careful choice of interpolation techniques in order to provide a numerical description of an airfoil.

The choice of a mathematical representation for an airfoil that is used in an aerodynamic design optimization process, along with the selection of the type of optimization algorithm, have a profound effect on such things as:

1) Computational time and resources
2) The extent and general nature of the design space and whether the geometries within in the design space are smooth or irregular, or even physically acceptable
3) If a meaningful "optimum" is contained in the design space
4) If an optimum design exists, can it be found?

The geometry representation method, can also affect the suitability of the selected optimization process. For example the use of discrete coordinates as design variables may not be suitable for use with a genetic optimization process since the resulting design space may be heavily populated with airfoils having bumpy irregular surfaces, thus making the possibility of locating an optimum smooth airfoil practically impossible.

Numerous methods [2, 3, 4, 5, 6, 7, 8] have been devised to numerically represent airfoil geometry for use in use in aerodynamic design, optimization and parametric studies. Some of these representation methods as shown in Fig. 2 include:

1) Sets of discrete airfoil coordinates as design variables
2) Bezier or B-Spline control point Representation
3) "Free form" airfoil representation by a set of control points as design variables
4) Numerically derived orthogonal basis functions
5) Polynomial Surface Representation.
6) Cubic Spline Control Point representation
7) Constant Thickness Distribution And Variable Camber Distribution and Angle of Attack.
8) Linear Shape Function Additions to a Reference Airfoil (eg. Hicks Henne functions)

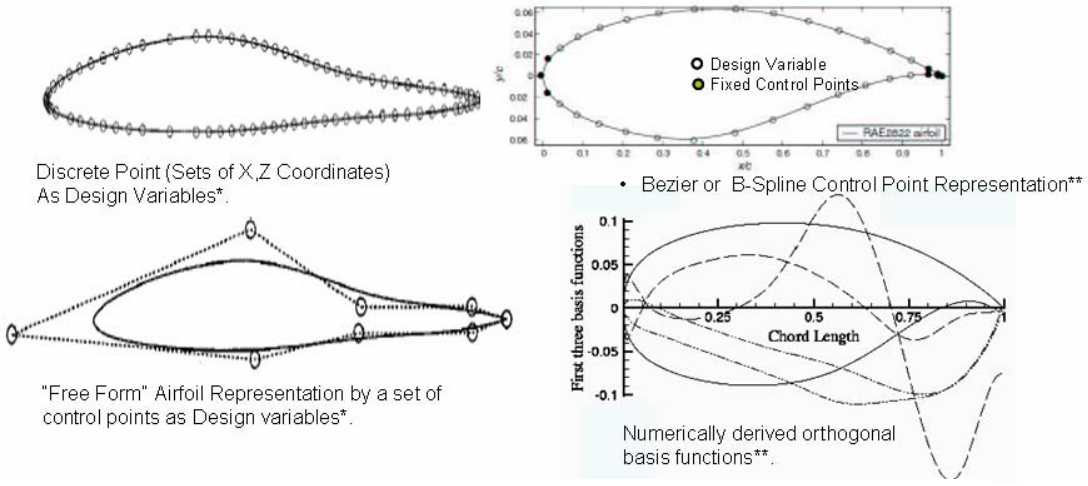

Figure 2: Various Airfoil Representation Schemes for Design Optimizations

The discrete approach is based on using a set of airfoil "x,z" coordinates as design variables. This approach is easy to implement, however a large number of coordinates are required, particularly near the nose of the airfoil. Consequently, the number of design variables is large and this may lead to a costly and as well as a difficult optimization problem to solve. Because the geometry is perturbed by moving individual grid points, a smooth geometry is difficult to maintain, and the optimized design may be impractical to manufacture. With this approach it is difficult to accurately represent or control the region near the airfoil nose.

Use of polynomial and spline representations for shape parameterization obviously can reduce the total number of design variables. The polynomial coefficients convey very little geometric insight about the shape. The polynomial or power basis form is prone to round-off error if there is a large variation in the magnitude of the coefficients. Because of the mathematical singularities near the airfoil nose, the nose shape of the starting airfoil is typically held constant and the design optimization process reshapes the airfoil only aft of the fixed nose section. Often, the geometry at the trailing edge is also held constant to insure airfoil closure.

The Bezier representation is another mathematical form for representing curves and surfaces. The Bezier form is a far better representation than the power basis, even though mathematically equivalent, The Bezier form is an effective and accurate representation for shape optimization of simple curves, Complex curves require a high-degree Bezier form. As the degree of a Bezier curve increases, so does the round off error. Also, it is very inefficient to compute a high-degree Bezier curve. Instead, of using a single Bezier representation for a complex curve, one can use several low-degree Bezier segments to cover the entire curve. The resulting composite curve is referred to as a spline or, more accurately, a B-spline. These methods also can not adequately represent the nose of an airfoil and therefore, typically require the assumption of fixed leading edge and fixed closure geometry.

Another method commonly used geometry method utilizes numerically derived orthogonal basis functions that are treated as perturbations to an initial baseline airfoil geometry. The design variables in this process are the scaling factors for each of the basis functions. All participating coefficients are initially set to zero, and so the first computation gives the baseline geometry. The shape functions are smooth functions based on a set of previous airfoil designs. This process is characterized by a very limited and rather unknown design space.

The "Free Form" method represents an airfoil by a set of control points as design variables. Each control point determines a local B-spline basis function. The design variables used in the free form method as shown in the Fig. may have no direct relationship to the actual airfoil geometry.

The following is a list of desirable features for any geometric representation technique.

1) Well behaved, and produce smooth and realistic shapes
2) Mathematically efficient and numerically stable process that is fast, accurate and consistent
3) Require relatively few variables to represent a large enough design space to contain optimum aerodynamic shapes for a variety of design conditions and constraints
4) Allows specification of key design parameters such as leading edge radius, boat-tail angle, airfoil closure.
5) Provide easy control for designing and editing the shape of a curve
6) Intuitive - Geometry algorithm should have an intuitive and geometric interpretation.
7) Systematic and Consistent - The way of representing, creating and editing different types of geometries must be the same.
8) Robust - The represented curve will not change its geometry under geometric transformations such as translation, rotation and affine transformations.

The previous described common geometry representation methods typically fail to meet the complete list of desirable features.

III. Airfoil Geometry Mathematical Description

In order to develop an improved airfoil geometry representation method, let us examine the fundamental geometric characteristics of a subsonic airfoil. The key design parameters for an airfoil, an axisymmetric nacelle, or body of revolution are all quite similar as shown in Fig. 3. The nose radius, R_{LE}, strongly affects the angle of attack capability before nose separation occurs on an airfoil, or crown line separation occurs on a nacelle. The forebody or forecowl shape, has a significant effect on the drag rise characteristics. The shape of the aftbody or aft cowl and the boattail closure angle, β, determine whether the flow remains attached to the aftbody or whether the flow separates. Consequently the aft body shape and boattail strongly affect the profile drag.

As previously mentioned, the objective of this study is to develop a simple, robust representation of an airfoil (body, nacelle) with only a "few" scalable parameters that captures a large design space for efficient aerodynamic design optimization and analysis. The approach that will be used, is to first develop the general mathematical equation that describes a round nose airfoil. We will then examine the mathematical equation in order to identify

grouping of terms or transformation, which will allow the representation of the complete geometry by well behaved mathematical analytic functions.

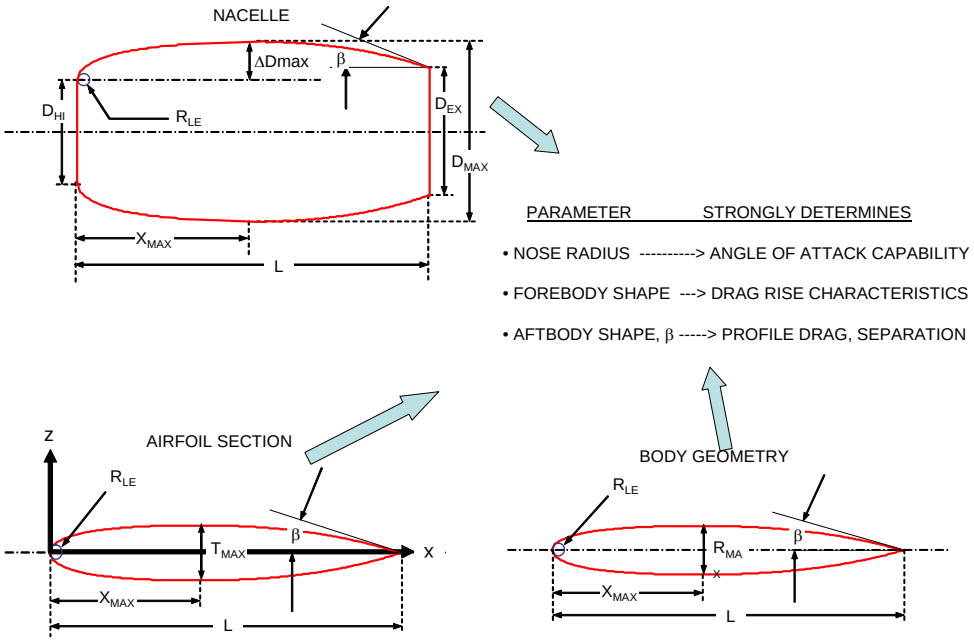

Figure 3. Airfoil, Axi-Symmetric Nacelle or Body Key Aerodynamic Design Parameters

The general round nose airfoil geometry shown in fig. 4 will be used for illustration purposes.

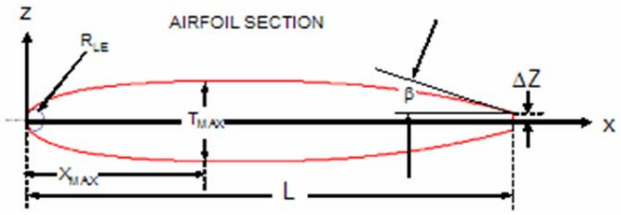

Figure 4. General Mathematical Description of a Blunt Base / Round Nose Airfoil

The general and necessary form of the mathematical expression that represents the airfoil geometry is:

$$\frac{z}{c} = \sqrt{\frac{x}{c}} \bullet \left(1 - \frac{x}{c}\right) \bullet \sum_{i=0}^{N} \left[A_i \bullet \left(\frac{x}{c}\right)^i \right] + \frac{x}{c} \bullet \frac{\Delta z_{TE}}{c} \qquad (1)$$

The only mathematical function that will provide a round nose is $\sqrt{\frac{x}{c}}$

The term $\left(1 - \frac{x}{c}\right)$ is required to insure a sharp trailing edge

The term $\frac{\Delta z_{TE}}{c}$ Provides trailing edge thickness

$\sum_{i=0}^{N}\left[A_i \bullet \left(\frac{x}{c}\right)^i\right]$ is a general function that describes the unique shape of the geometry between the round nose and the sharp aft end

A. Airfoil Shape Function

The source of the non-analytic characteristic of the basic airfoil equation is associated with the square root term in equation 1. Let us define the shape function "S" that is derived from the basic geometry equation by first subtracting the trailing edge thickness term and then dividing by the round nose and sharp end terms.

This gives:

$$S\left(x/c\right) \equiv \frac{\frac{z}{c} - \frac{x}{c}\frac{\Delta z}{c}}{\sqrt{\frac{x}{c}} \bullet \left[1 - \frac{x}{c}\right]} \tag{2}$$

The equation that represents the "S" function becomes the rather simple equation:

$$S\left(x/c\right) = \sum_{i=0}^{N}\left[A_i \bullet \left[\frac{x}{c}\right]^i\right] \tag{3}$$

The function representing the unique airfoil shape is shown here as a polynomial for convenience. However as will be shown later any desired mathematical approximation can be used. The significant feature of the "shape function" is that it is a well behaved analytic function. It ia shown in the appendix, that leading edge radius, the trailing edge thickness and the boat-tail angle are directly related to the bounding values of the shape function. The value of the shape function at x/c = 0 is directly related to the airfoil leading edge nose radius by the relation:

$$S\left(0\right) = \sqrt{2\,R_{LE}/c} \tag{4}$$

The value of the shape function at x/c = 1 is directly related to the airfoil boattail angle and trailing edge thickness by the relation:

$$S\left(1\right) = \tan\beta + \frac{\Delta Z_{TE}}{c} \tag{5}$$

Hence, in the transformed coordinate system, specifying the endpoints of the "S" function provides and an easy way to define the leading radius and the closure boattail angle.

The term $\sqrt{\frac{x}{c}} \bullet \left[1 - \frac{x}{c}\right]$ will be called the "class function", C(x/c), and is defined in the general form as:

$$C\left(x/c\right) = \left(\frac{x}{c}\right)^{N1}\left[1 - \frac{x}{c}\right]^{N2} \tag{6}$$

For a round nose airfoil N1 = 0.5 and N2 = 1.0. It will be subsequently shown that the exponents of the class function define basic general classes of geometric shapes.

The coordinates for an airfoil shape can be easily obtained from a known shape function and class function as:

$$\frac{z}{c}\left(x/c\right) = C\left(x/c\right) \bullet S\left(x/c\right) + \frac{x}{c} \bullet \frac{\Delta z}{c} \tag{7}$$

Similarly, the shape function for a specific airfoil can be calculated from the airfoil ordinates and the class function using equation 2.

An example of the transformation of the actual airfoil geometry to the corresponding shape function is shown in Fig. 5. The transformation of a constant Zmax and constant boat-tail angle lines are also shown as curves in the transformed plane.

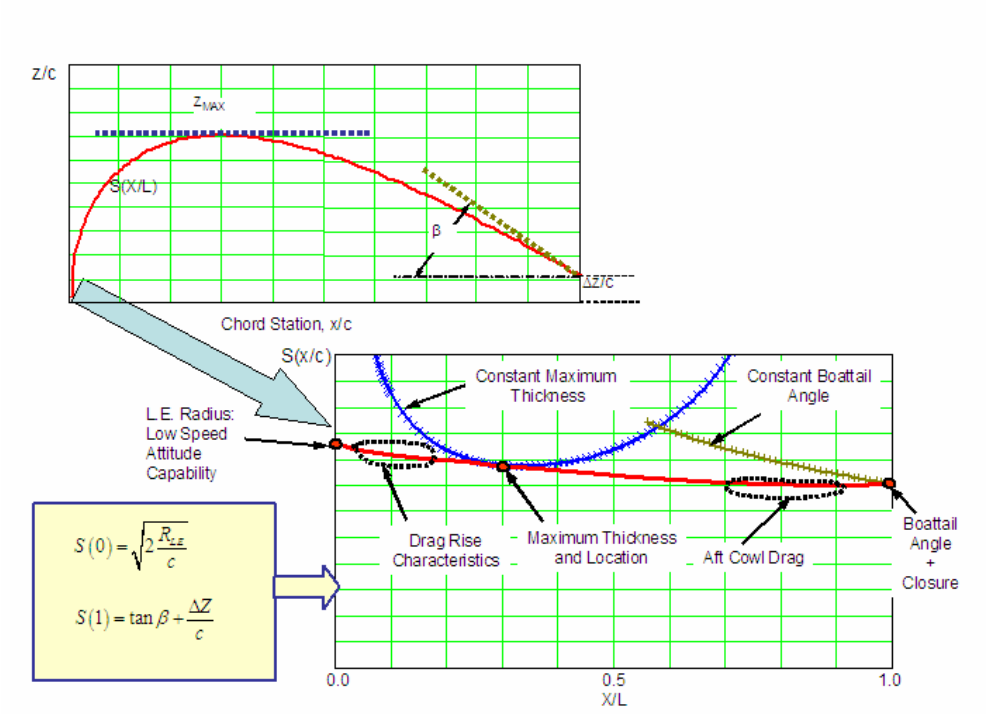

Figure 5. Example of an Airfoil Shape Function and Airfoil Design Guidelines

The shape function for this airfoil is seen to be approximately a straight line with the value at zero related to the leading edge radius of curvature and the value at the aft end equal to tangent of the boattail angle plus the ratio of base thickness / length. It is readily apparent that the shape function is indeed a very simple analytic function.

The areas of the airfoil that affect the drag and aerodynamic performance characteristics are readily visible on the shape function are also shown in Fig. 5. The shape function therefore, provides both visibility and easy control of the airfoil critical design parameters.

Fig. 6 contains examples of the shape functions for a variety of geometries.

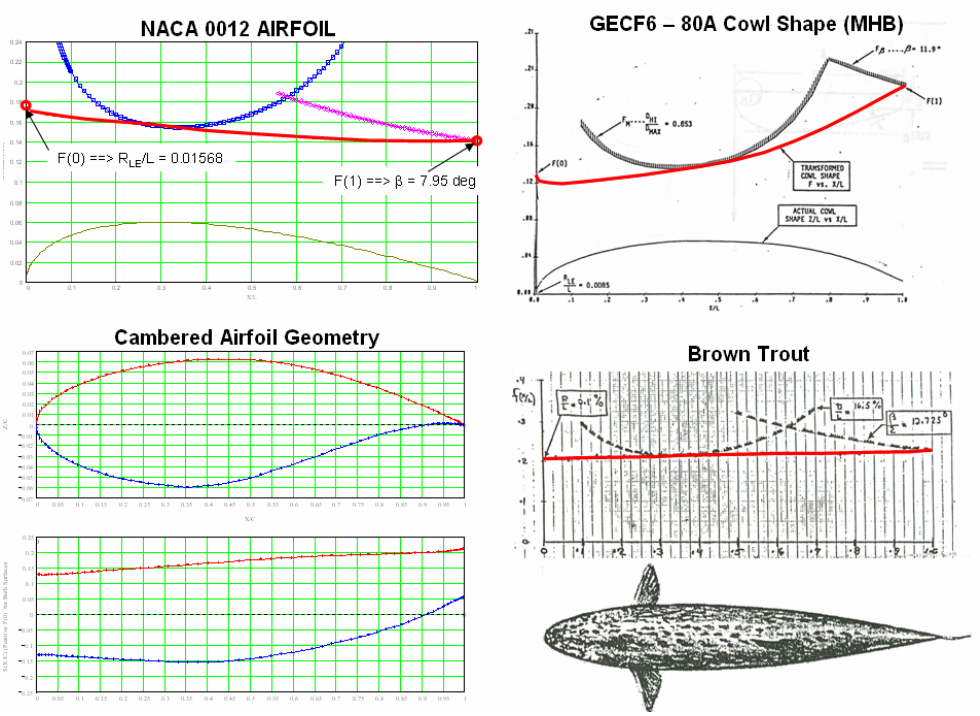

Figure 6. Examples of Various Shape Functions

The shape function for the NACA0012 airfoil is very nearly a straight line. The shape function for the CF6-80A has very sight curvature with a tiny hook near the leading edge of the airfoil which would produce a slight increase in the leading edge radius. The third Fig. shows the shape functions for the upper and lower surfaces of a cambered airfoil. The magnitudes of the shape functions for the upper and lower surface of at the nose of the airfoil are equal. This indicates that the leading edge radius is continuous around the leading edge.

The shape function for a brown trout is also shown in the figure. Nature appears to favor simple shape functions.

IV. Representing the Shape Function of an Airfoil

The method proposed in this report is to use the mathematically simpler shape function to represent an airfoil for design and or analysis studies. We will now explore a variety of techniques that can be used to represent the shape function of an airfoil for design or optimization studies.

Fig. 7 shows the fundamental baseline airfoil derived from the simplest of all shape functions, the unit shape function: S(x) = 1.

Simple parametric variations of the unit shape function are also shown in the figure along the corresponding changes of the airfoil geometry. The parametric variations control four key airfoil design variables:

1) Leading edge radius
2) Trailing edge boattail angle
3) Maximum thickness
4) Location of maximum thickness

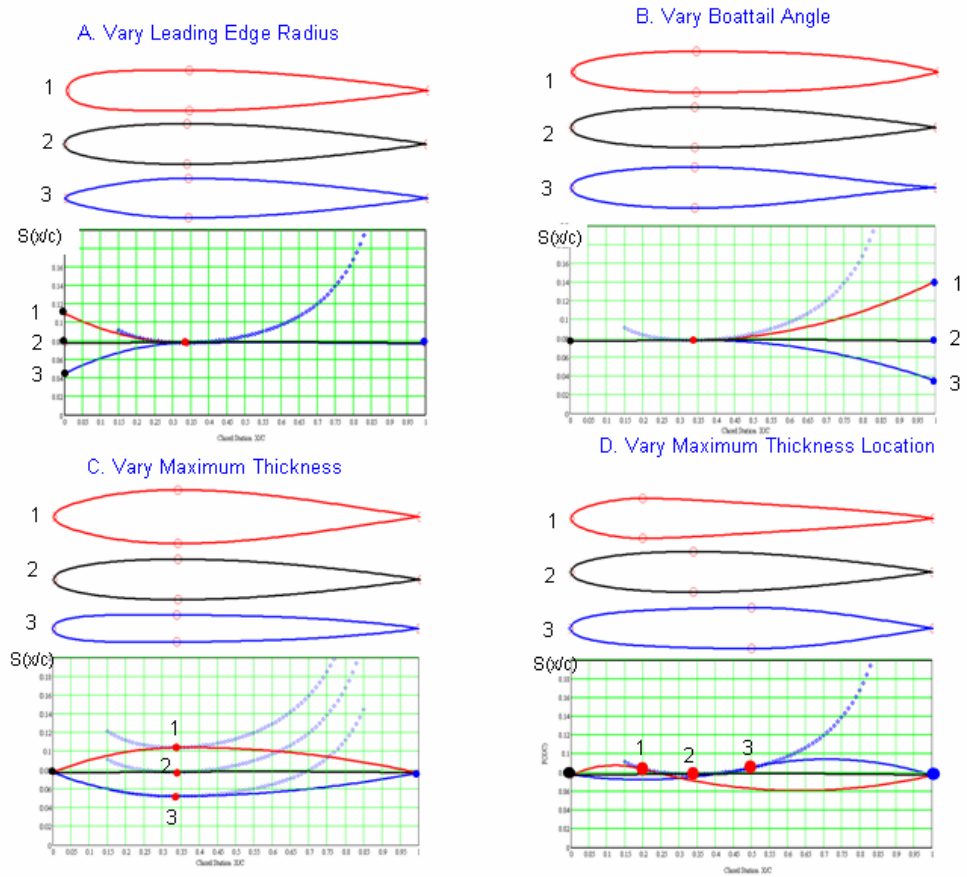

Figure 7. Examples of One Parameter Airfoil Variations

Figure 7A shows changes in the leading edge radius and the front portions of the airfoil and nacelle obtained by varying the value of S(0) with a quadratic equation that is tangent to the Zmax curve at x/c for Zmax. The maximum thickness, maximum thickness location and boattail angle consequently, remained constant. Figure 7B shows variations in boattail angle obtained by changing the value of the shape factor at the aft end, x/c = 1, while the front

of the airfoil is unchanged. Figure 7C shows variations in maximum thickness while maintaining a constant leading edge radius and a constant boattail angle. Figure 7D shows variations in the location of maximum thickness while in both cases the leading edge radius and trailing edge boattail angle are both held constant. In each of these examples the airfoil shape changes are controlled by a single variable and in all cases the resulting airfoil is both smooth and continuous.

As previously mentioned, the values of the exponents N1 and N2 of the class function, define the basic class of geometries. In Fig. 8, various geometries are shown that can be obtained with the unit shape function [S(x)=1.0] but different class functions.

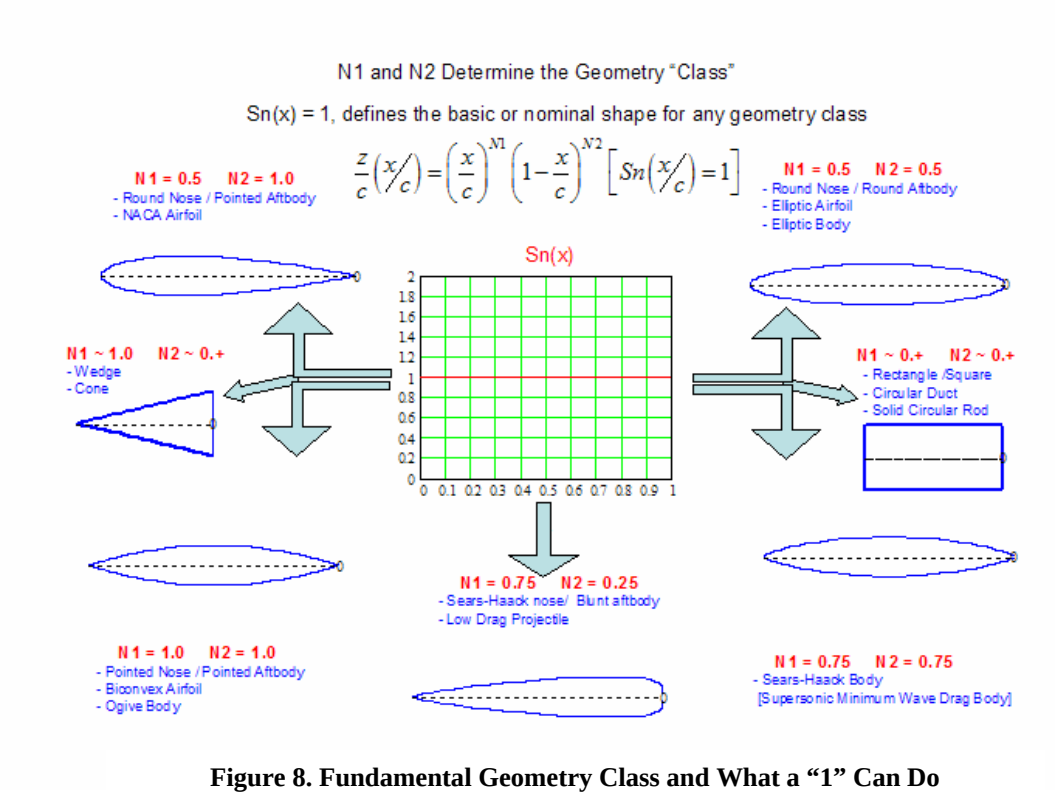

Figure 8. Fundamental Geometry Class and What a "1" Can Do

1) The values of N1 = 0.5 and N2 = 1.0 results in a NACA type round nose and pointed aft end airfoil.
2) The values of N1 = 0.5 and N2 = 0.5 results in a round nose / round aft end elliptic airfoil, or an ellipsoid body of revolution
3) The values of N1 = 1.0 and N2 = 1.0 results in a biconvex airfoil pointed nose and pointed aft-end airfoil, or an ogive body.
4) The values of N1 = 0.75 and N2 = 0.75 results in a Sears-Haack body which is the supersonic minimum wave drag body shape for a given volume.
5) The values N1 = 0.75 and N2 = 0.25 results in a low drag projectile
6) Values of N1 = 1.0 and N2 = 0.0001+ results in a cone or wedge airfoil.
7) Values of N1 = 0.0+ and N2 = 0.0001 results in a rectangle, circular duct or circular rod.

For any class, the geometry corresponding to the unit shape function, S(x) =1, is called the basic or nominal shape for that class

A. Airfoil Decomposition into Component Shapes

In Fig. 9 it is shown that the unit shape function defined by S(x/c) = 1, can be decomposed into two component shape functions: S(x/c) = S1(x/c) + S2(x/c)

S1(x/c) = 1-x/c

S2(x/c) = x/c

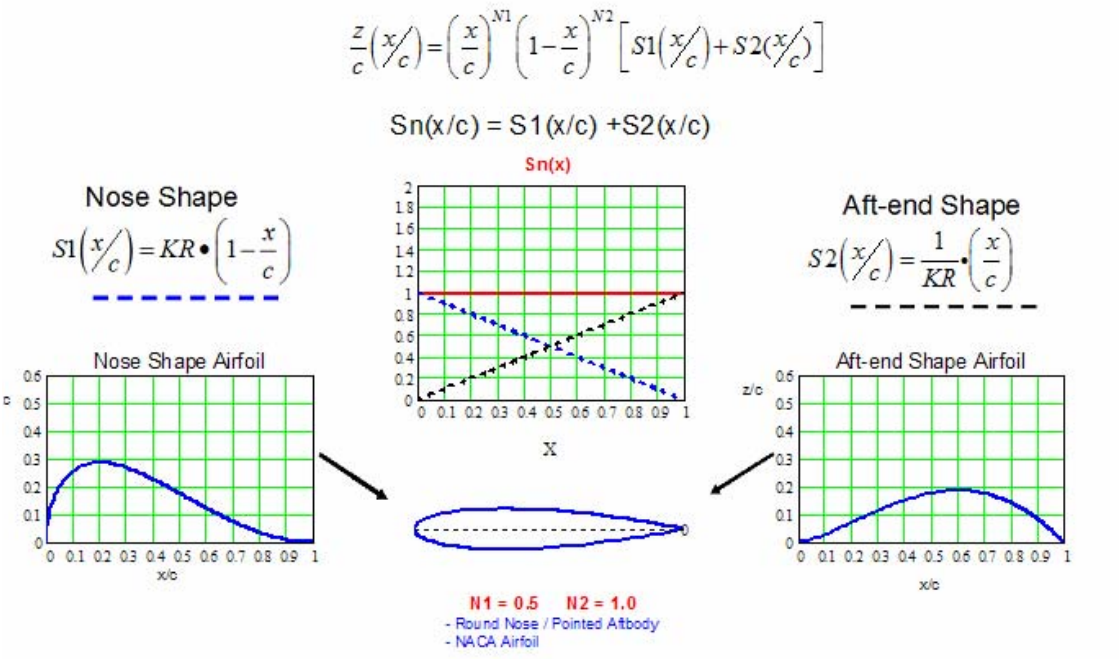

Figure 9. Airfoil Decomposition into Component Shapes or Basis Functions

The airfoil geometries corresponding to each of these component shape functions are also shown. The first component shape function, S1(x/c), corresponds to an airfoil with a round nose and zero boattail angle. The second component airfoil, S2(x/c), corresponds to an airfoil with zero nose radius and a finite boattail angle.

In fig. 10 an arbitrary scaling factor KR factor is introduced. By varying the scaling factor, KR, the relative magnitudes of the leading edge radius and the boattail angle can be changed. This results in a family of airfoils of varying leading edge radius, boattail angle and location of maximum thickness. All these variations are controlled by the single parameter KR. An example of a typical airfoil variation is shown in the figure.

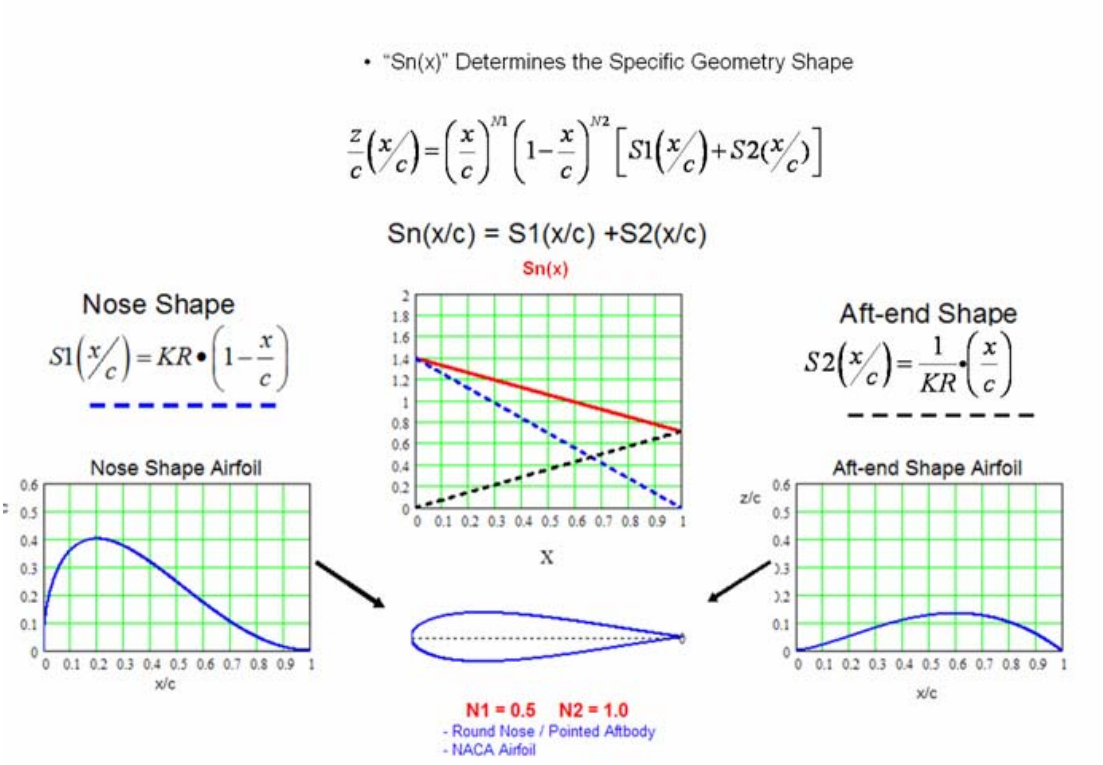

Figure 10: Airfoil Shape Change by Varying Component Shape Functions

The unit shape function, as well as the previously shown decomposition of the unit shape function into two component shape functions as shown in fig. 11, have simple mathematical interpretations as the zero order and first order Bernstein polynomials.

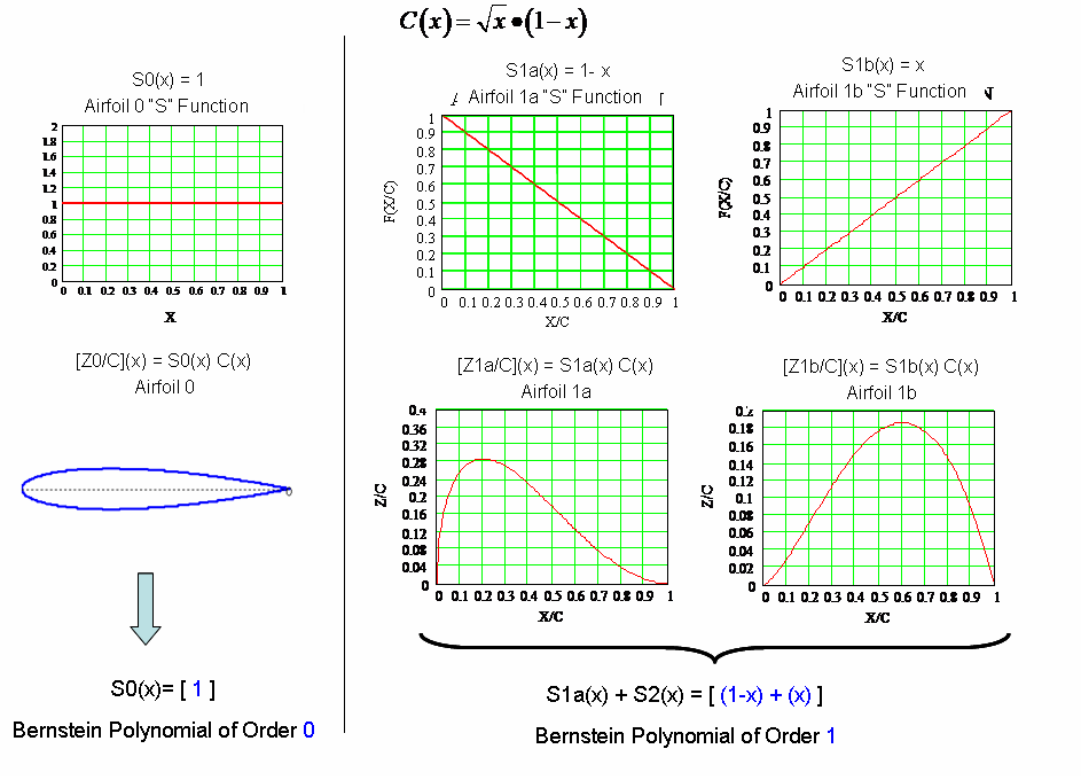

Figure 11. Unit Airfoil Representation by Composite Airfoils

The definition of the Bernstein polynomial of order n, BPn, is:

$$BPn = \sum_{r=0}^{n} K_{r,n} x^r \left(1-x\right)^{n-r} \tag{8}$$

The variable x is limited to values from 0 to 1

The coefficients factors $K_{r,n}$ are binominal coefficients defined as:

$$K_{r,n} \equiv \binom{n}{r} \equiv \frac{n!}{r!(n-r)!} \tag{9}$$

The individual terms in increasing orders of Bernstein polynomials of can be illustrated by means of Pascal's triangle as shown in fig. 12. It is seen in the figure, that a Bernstein polynomial of order n consists of "n+1" terms defined as:

$$S_{r,n}(x) = K_{r,n} x^r \left(1-x\right)^{n-r} \tag{10}$$

Bernstein polynomials have the mathematical property of "Partition of Unity" since every for every order n:

$$BPn = 1 \tag{11}$$

Consequently, the unit shape function can be represented by increasing orders of Bernstein polynomials. This provides a systematic process to decompose the unit shape function into increasing numbers of component shapes.

As shown in fig.12, for any order of Bernstein polynomial selected to represent the unit shape function, only the first term defines the leading edge radius and only the last term defines the boattail angle. The other in-between terms are "shaping terms" that neither affect the leading edge radius nor the trailing edge boattail angle.

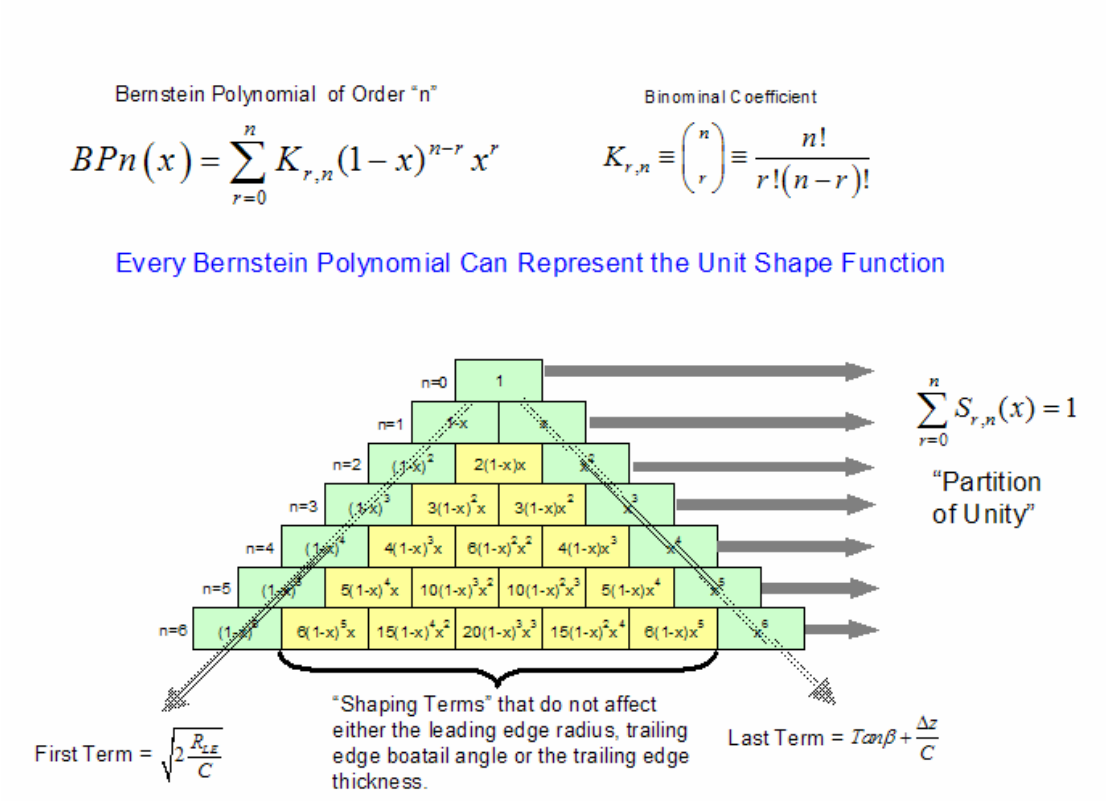

Figure 12. Bernstein Polynomial Representation of the Unit Shape Function

Representations of the unit shape function using various orders of Bernstein polynomials are shown in fig. 13 along with the corresponding component airfoils.

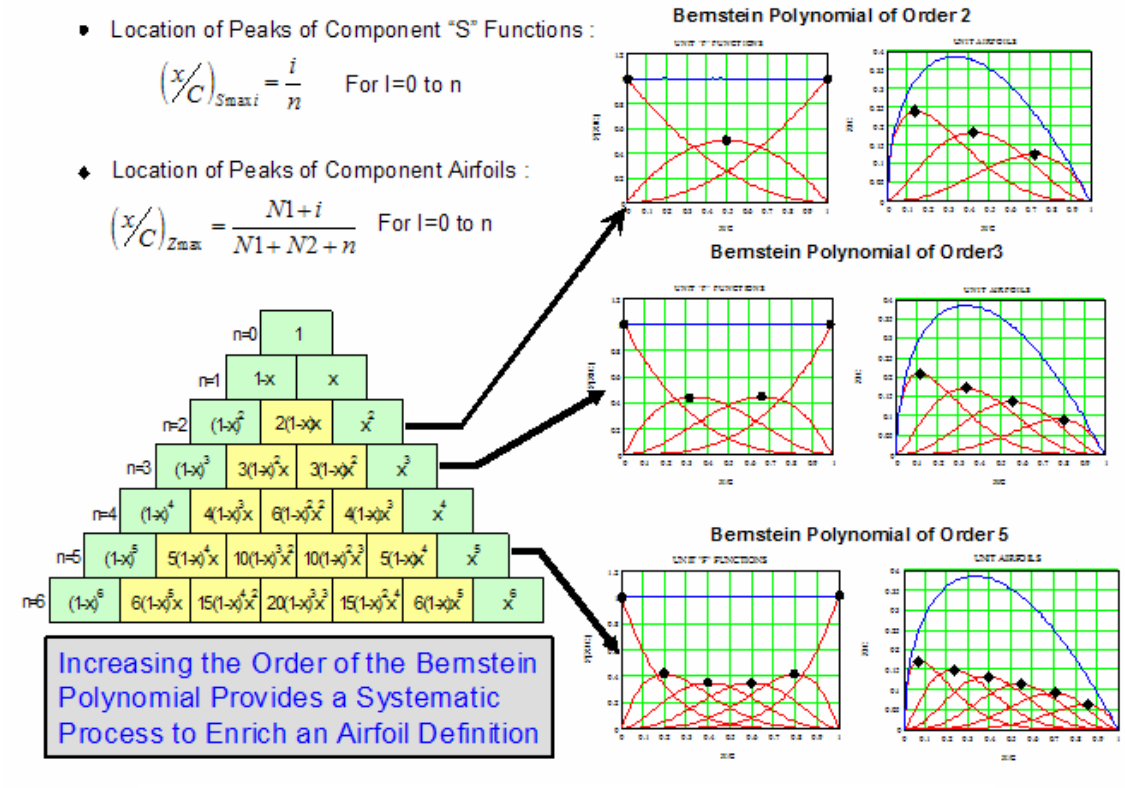

Figure 13. Bernstein Polynomial Provides "Natural Shapes"

The locations of the peaks of the component "S" functions are equally spaced along the chord at stations that are defined by the equation:

$$\left(x/C\right)_{S\max i} = \frac{i}{n} \tag{12}$$

The corresponding locations of the component airfoils are also equally spaced along the chord of the airfoil and are defined in terms of the class function exponents and the order of the Bernstein polynomial by the equation:

$$\left(x/C\right)_{Z\max} = \frac{N1+i}{N1+N2+n} \tag{13}$$

In eq. 12 and eq. 13, i = 0 to n

B. Airfoils Defined Using Bernstein Polynomials Representation of the Unit Shape Function

The upper and lower surfaces of an airfoil can each be defined using Bernstein Polynomials of any order n, to represent of the shape function for each surface, multiplied by the class function.

Upper surface definition:

$$\left(\xi\right)_{Upper} = C\left(\psi\right) \bullet Su\left(\psi\right) + \psi \bullet \Delta\xi_{Upper} \tag{14}$$

$$Su\left(\psi\right) = \sum_{i=1}^{n} Au_i \bullet S_i(\psi) \tag{15}$$

Lower surface definition:

$$\left(\xi\right)_{Lower} = C\left(\psi\right) \bullet Sl\left(\psi\right) + \psi \bullet \Delta\xi_{Lower} \tag{16}$$

$$Sl\left(\psi\right) = \sum_{i=1}^{n} Al_i \bullet S_i(\psi) \tag{17}$$

The class function is:

$$C\left(\psi\right) = \psi^{Nnose} \bullet \left(1-\psi\right)^{Naft} \tag{18}$$

The various terms in eq. 14 through eq. 18 are defined as:

Non-dimensional airfoil station: $\psi = \frac{x}{C}$

Non-dimensional airfoil ordinate: $\xi = \frac{z}{C}$

Non-Dimensional upper surface trailing edge thickness ratio: $\Delta\xi_U = \frac{zu_{TE}}{C}$

Non-dimensional lower surface trailing edge thickness ratio: $\Delta\xi_L = \frac{zl_{TE}}{C}$

The individual terms of the Bernstein polynomials are scaled by the "to be determined" coefficients "Aui" and "Ali". The coefficients Aui and Ali can be determined by a variety of techniques depending on the objective of the particular study. Some examples include:

1) Variables in a numerical design optimization application
2) Least squares fit to match a specified geometry
3) Parametric shape variations

In any desired application the upper and lower surface leading edge radii can be required to be equal and therefore provide continuity in curvature around the leading edge by simply requiring that :

$$Au_{i=0} = Al_{i=0} \tag{19}$$

C. **Weirstrass Theorem and Bernstein Polynomials**

The airfoil shape function "S(x)" for any continuous airfoil is a smooth continuous and analytic function with finite derivatives of any order over the entire surface of the airfoil. We can therefore, utilize the Weirstrass theorem

to establish the universality of the newly defined airfoil representation technique consisting of the class function, plus the Bernstein Polynomial, BP, representation of the shape function.
The Weirstrass theorem is stated as:

1) Let PM(x) be an Mth degree polynomial approximating the function S(x) over the interval [a,b]

2) Define the error between the approximating and actual function, e(x), as

$$e(x) = PM(x) - S(x)$$

3) Since S(x) is a continuous analytic function over the interval [a,b], then there is a polynomial of sufficiently high degree M so that $|e(x)| < e$ for any value of x between a and b where e is an arbitrary positive tolerance.

In our application [a,b] = [0,1].

Consequently the "Class Function" / "Shape Function" airfoil representation method utilizing Bernstein polynomials has the following unique and very powerful properties:

1) Any smooth airfoil can be represented as "exactly" as desired

2) This airfoil representation technique therefore, captures the entire design space of smooth airfoils

3) Every airfoil in the entire design space can be derived from the unit shape function airfoil

4) Every airfoil in the design space is therefore derivable from every other airfoil

V. Airfoil Representation ➔ Key Convergence Question

A key convergence question relative to the class function / shape function geometry method for defining airfoils, nacelles or bodies of revolution is the following. What orders of Bernstein polynomials, BPO, are required to capture enough of a meaningful design space to contain a true optimum design?

A three step approach was defined in order to obtain the answer for this question:

1) Compare actual airfoil and represented airfoil geometries for a wide variety of airfoils
- Use various orders of Bernstein polynomials for the shape function to approximate the actual airfoils shape functions computed from the defined airfoil coordinates. The coefficients for the component Bernstein polynomial shape functions were to be determined by least squares fits to the selected airfoil upper and lower surface shape functions.
- Investigate a wide variety of optimum and non-optimum, symmetric and cambered airfoil geometries.
- Compute the statistical measures such as "residual differences", "standard deviations" and "correlation functions" to quantify the "mathematical goodness" of the representations for each of the study airfoils.
- Compare surface slopes, 2nd derivatives and curvature between actual and approximate airfoil shapes

2) Conduct TRANAIR with boundary layer CFD analyses of the actual and the corresponding shape function defined airfoils. The CFD analyses for each study airfoil was to use the actual airfoil defining stations.

3) Conduct TRANAIR optimization with shape function coefficient variables for increasing order of Bernstein polynomials.

The results of steps 1 and 2 will be summarized in this paper.

More than 30 airfoils have been analyzed applying steps 1 and 2. These include symmetric NACA airfoils, cambered NACA airfoils, high lift airfoils, natural laminar flow airfoils, shock-free airfoils, supercritical airfoils and transonic multipoint optimized airfoils. Results of the analyses of some of these airfoils will be shown to illustrate the evaluation processes and to demonstrate the rate of convergence of a Bernstein Polynomial shape function airfoil representation, to the corresponding specified airfoil geometry with increasing orders of BPO.

A. NACA0012 Symmetric Airfoil Study

Fig. 14 shows the NACA0012 airfoil and the corresponding shape function computed from the 352 airfoil defining ordinates. The shape function curve is a very "simple" curve as compared to the actual airfoil shape.

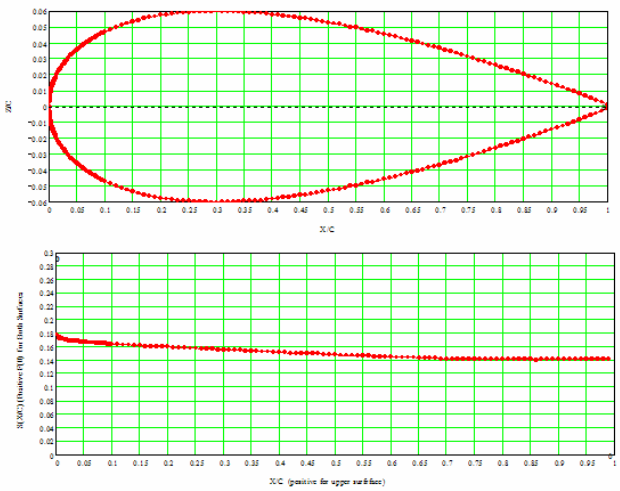

Figure 14. NACA0012 Symmetric Airfoil – (Defined by 352 "X, Z" Coordinates)

The convergence studies for the NACA0012 airfoil included very detailed comparisons of the geometric and aerodynamic characteristics of the NACA0012 airfoil with those calculated for 14 approximate airfoils obtained with BPO = 2 to BPO = 15 shape functions. Shape functions calculated by the method of least squares corresponding to increasing orders of Bernstein's polynomials, are compared with the shape function determined from the actual NACA0012 geometry in fig. 15.

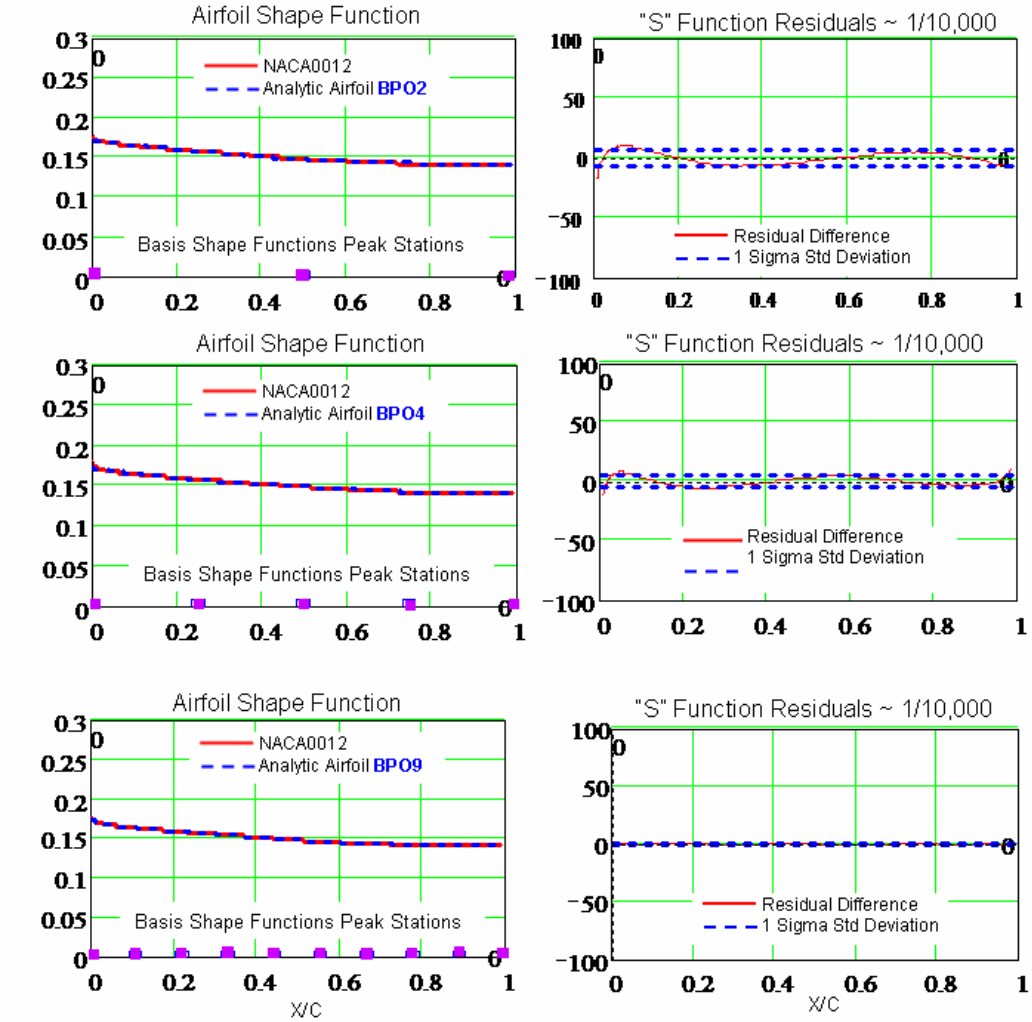

Figure 15. Effect of BPO on Representation of NACA0012 Symmetric Airfoil Shape Function

The locations of the peaks of the basis shape functions and are indicated on the figures. The residual differences between the approximated and the official shape functions are also shown. For this example, the differences between the shape functions for the actual geometry and the approximated geometries are hardly discernible even for the Bernstein Polynomial of order 2, BPO2, airfoil definition. The corresponding airfoil coordinate comparisons are shown in fig.16 along with the residual differences between the approximated airfoils and the actual airfoil geometry. The z/c residuals are shown as z/c x 10^4. Typical wind tunnel model tolerances are also shown in the z/c residual plots. The oscillating nature of the residual curves is typical of any least squares fit. All of the residual differences shown in the figure are less than the wind tunnel model tolerances. The tighter tolerance for x/c $\leq$ 20%, is less than the thickness of a piece of printer paper.

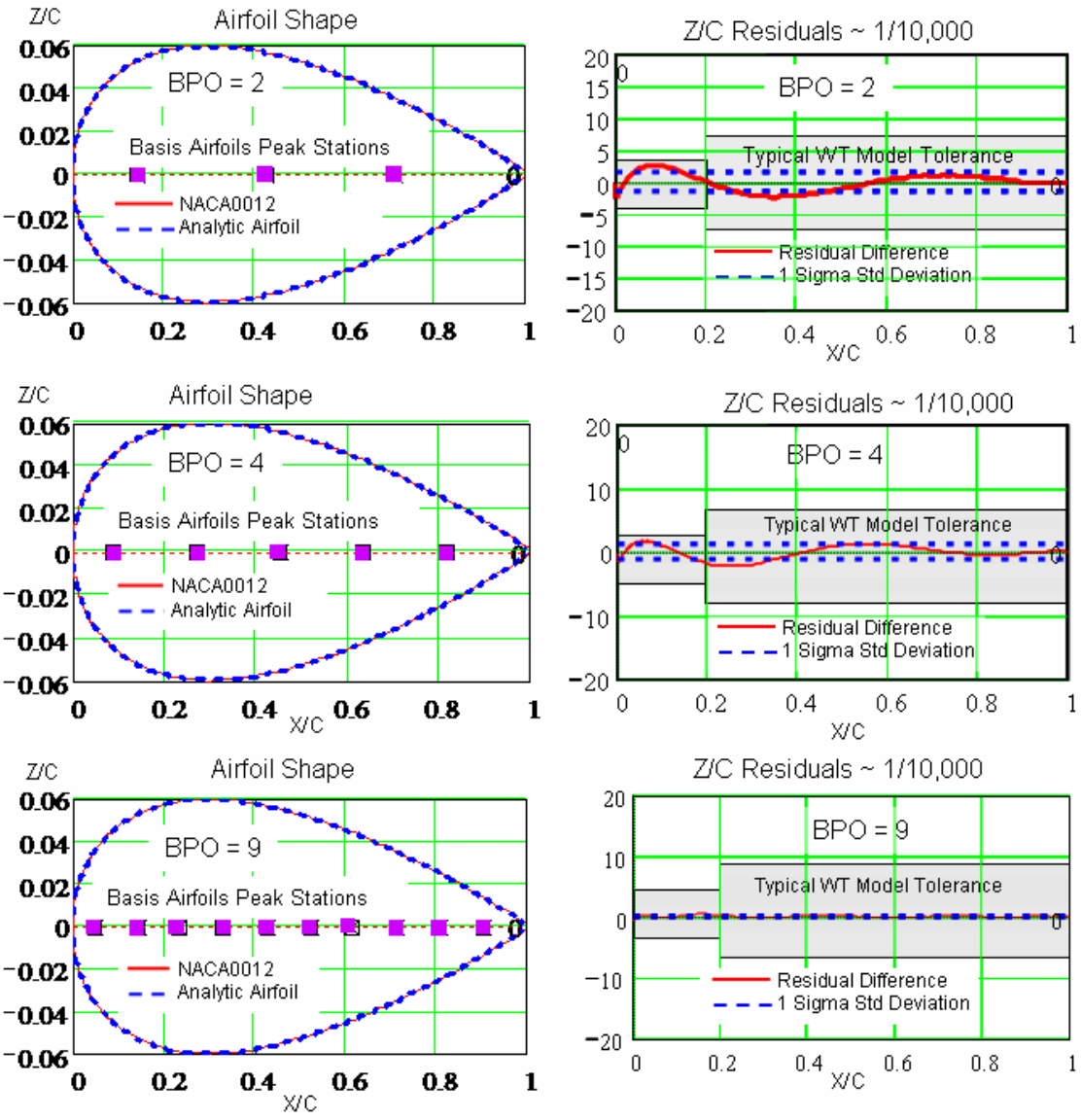

Figure 16. Effect of BPO on Representation of NACA0012 Symmetric Airfoil Geometry Coordinates

The NACA0012 airfoil and the approximate airfoil obtained with a Bernstein's Polynomial of Order 2, (BPO2) agree very closely with the actual airfoil geometry as shown in fig. 16. The results obtained with BPO4 and PBO9 show that the residual differences rapidly vanish with increasing order of the representing Bernstein polynomial.

The slopes and 2nd derivatives obtained with various orders of BP shape functions are compared with slopes and 2nd derivatives obtained from the NACA0012 airfoil coordinates in fig. 17.

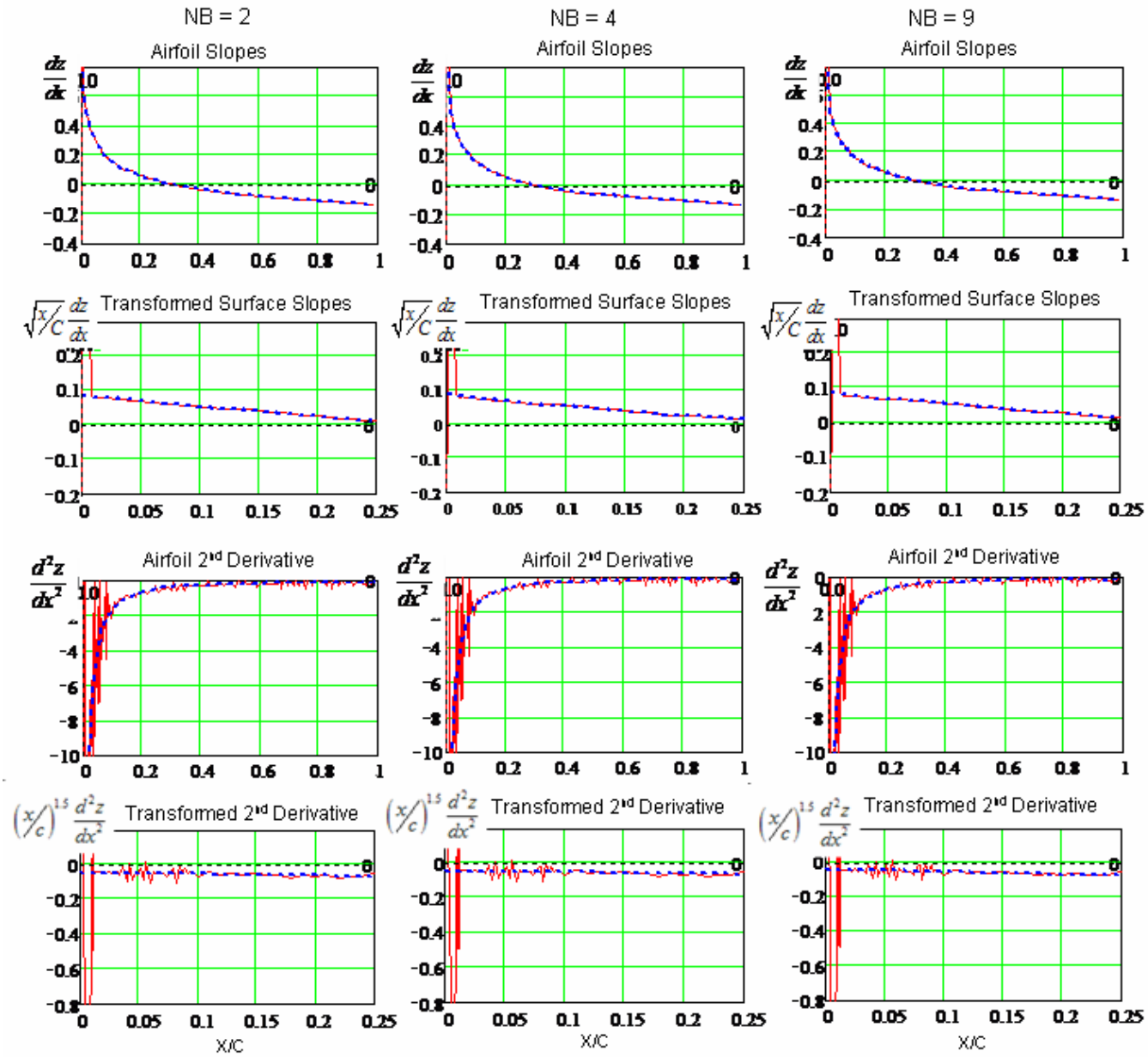

Figure 17. Effect of BPO Representation of NACA0012 Symmetric Airfoil on Slopes and 2nd Derivatives

The airfoil slopes and 2nd derivatives both numerically go to infinity near the nose of the airfoil and therefore it is difficult to see differences between matched geometry and actual airfoil geometry in the nose region.

The singularity in the 1st derivative can be eliminated through the use of a transformed slope obtained by multiplying the slope by $(x/c)^{0.5}$. Similarly the singularity in the second derivative can be removed by multiplying the 2nd derivatives by $(x/c)^{1.5}$.

As shown in the figure, the values of the transformed slopes and 2nd derivative at the leading edge are both related to the airfoil leading edge radius.

$$\sqrt{\frac{x}{c}}\frac{dz}{dx}_{x/c\Rightarrow 0} = \sqrt{\frac{1}{2}\frac{R_{LE}}{c}} \tag{20}$$

And

$$\left(\frac{x}{c}\right)^{1.5}\frac{d^2z}{dx^2}_{x/c\Rightarrow 0} = \sqrt{\frac{1}{8}\frac{R_{LE}}{c}} \tag{21}$$

The irregularities in the 1st and 2nd derivatives computed from the NACA0012 airfoil coordinates are likely due to round off effects of the tabulated "x/c, z/c" defining coordinates. The derivatives obtained from the shape function defined geometries show the powerful smoothing effect inherent in the shape function defined airfoils.

Two statistical measures of the quality of the shape function represents of the NACA0012 airfoil geometry are shown in fig. 18 as a function of the order of the Bernstein polynomial. These include "1 sigma" standard deviation of the residuals for both the shape function and airfoil coordinates, and the correlation coefficient, r^2, which is expressed here in terms of a correlation factor which is defined as:

$$\text{Correlation Factor} = -\log(1-r2) \tag{22}$$

The correlation factor equals the number of initial "9"s in the correlation coefficients between the airfoil data and the corresponding approximated data. For example a correlation factor of 5.0 means that r2 = 0.99999

The results in the figure show even the low orders of the BPO representations of the shape function result in airfoils that are nearly exact representations of the NACA0012 geometry.

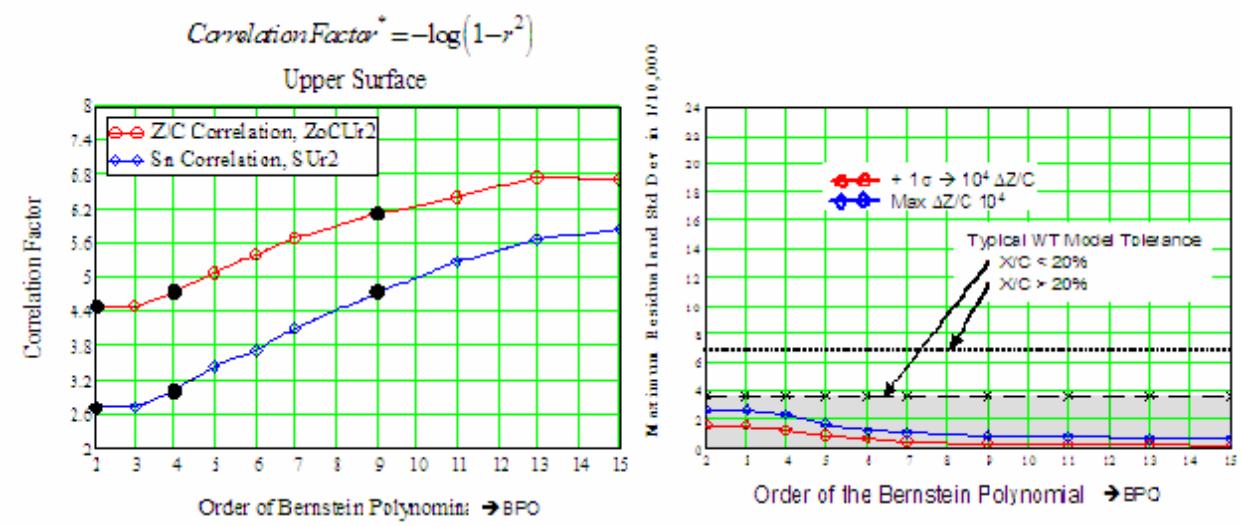

Figure 18. Statistical Convergence of NACA0012 Airfoil With Increasing BPO

B. TRANAIR Force and Pressure Predictions

The 2nd previously described step in the process to determine the order of Bernstein polynomial representation of the shape function necessary to adequately match the actual airfoil geometry, involved detailed CFD analyses of actual and approximate airfoil geometries and then comparing the calculated surface pressure distributions and aerodynamic forces.

CFD analyses were made with the TRANAIR full potential code with boundary layer. TRANAIR [9, 10, 11, 12] solves the full potential equation on a hierarchically-refined Cartesian grid. An initial (typically uniform) global Cartesian grid is used with a finite element discretization to obtain solutions to the full potential equation. Based upon solution gradients, the grid is refined by each cell where gradients are large into four cells (in 2D). The process proceeds through of the order of ten cycles. Cells which contain a portion of the boundary are discretized in a special way such that the finite element integrations are only performed over the "external" portion of the cell area. This allows a high degree of independence between the surface and volume grids. The surface discretization can be used to define an integral boundary layer grid. Based upon solutions to the integral boundary layer equations, transpirations are computed and imposed to represent the displacement effect of the viscous flow. The solutions of the coupled boundary layer/full potential system are obtained as a fully coupled system of equations using Newton's method. Linear solutions are obtained using a preconditioned GMRES algorithm that uses an incomplete factorization of the sparse matrix representing the whole system of equations as a preconditioner. Typically

convergence of the system of equations is obtained in ten to twenty Newton steps on each grid. Grid sizes grow by about a factor of two for each adaptive cycle.

The analysis grid for the NACA0012 TRANAIR analyses is shown in fig. 19.

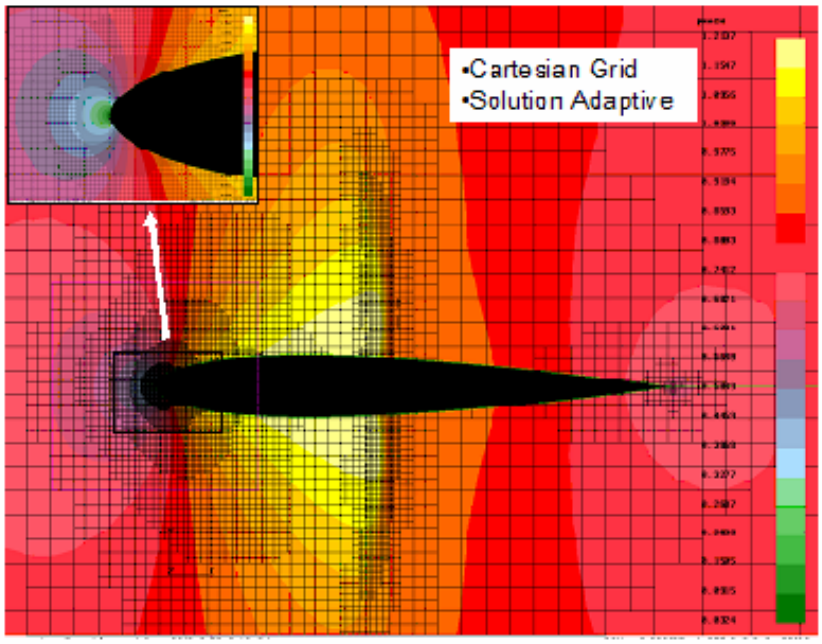

Figure 19. TRANAIR Full Potential Code + Boundary Layer: Computational Adaptive Grid

The wave drag and profile drag calculations for the NACA0012, and for the approximating airfoils corresponding to different orders of PB representations are shown in fig. 20. The calculations were obtained using the TRANAIR full potential code for a Mach number of 0.79, zero degrees angle of attack, and a chord Reynolds number of 10^7.

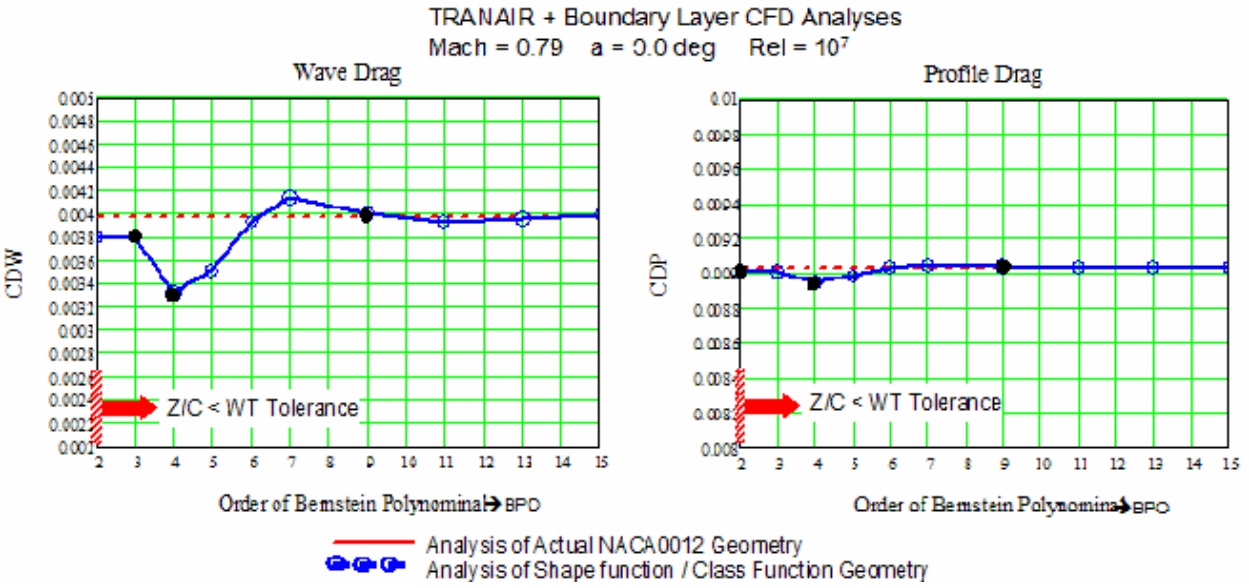

Figure 20. NACA0012 Symmetric Airfoil Drag Convergence Study

The profile drag predictions for all orders of BP representations are all close to the NACA0012 prediction. The wave drag predictions for BP orders of 6 or above match the NACA0012 prediction. This is not surprising since as previously shown, these representations of the NACA0012 are nearly statistically exact. The predictions for the lower BP representations for the most part, are less than the NACA0012 prediction. The wave drag for the BPO4 airfoil is significantly lower drag airfoil than that for the NACA0012, even though as shown in the previous figures the differences between the NACA0012 geometry and the lower BP representations are difficult to discern and are within typical wind tunnel model tolerances.

The slopes, 2nd derivatives and curvature for the NACA0012 are compared with the slopes, 2nd derivatives and curvature of the corresponding shape function for the airfoil, in fig. 21.

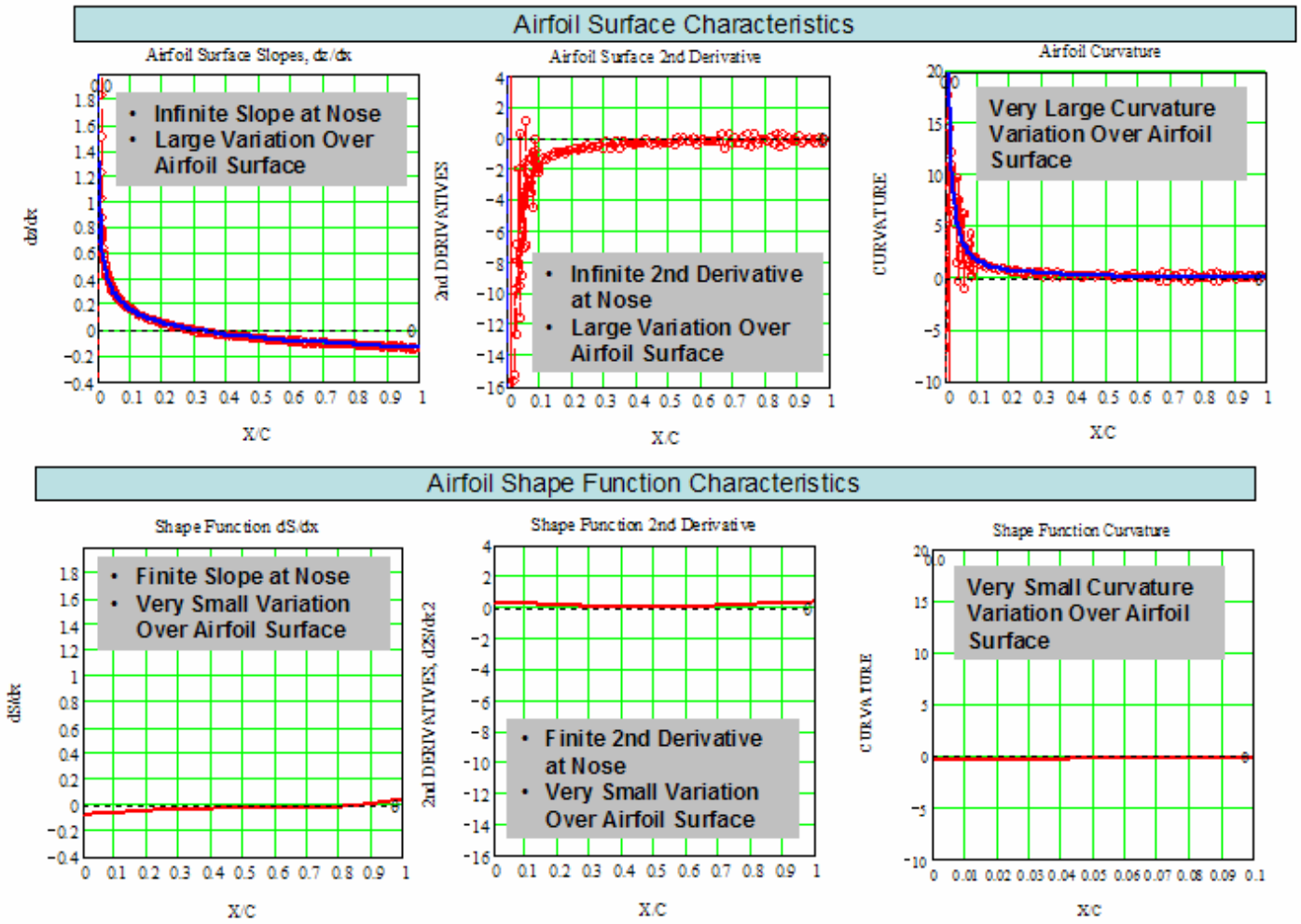

Figure 21. Mathematical Simplicity of the Shape Function – NACA0012

The slopes and second derivatives of the NACA0012 airfoil are infinite at the nose, and the curvature varies greatly over the surface of the airfoil. The slopes and 2nd derivatives are finite, and every where small for the NACA0012 shape function, and the curvature of the shape function is essentially zero. This clearly shows the distinct advantage of mathematical simplicity that the shape function airfoil representation methodology has relative to the use of the actual coordinates of the airfoil.

C. RAE 2822 Cambered Airfoil Study

Fig. 22 shows the geometry of the RAE 2822 airfoil as defined by 130 "x,z" coordinates, and the corresponding shape functions for the upper and lower surfaces. This is one of approximately 25 different cambered airfoils that were used to evaluate the effectiveness of the shape function / class function analytic method for representing airfoils. The RAE 2822 airfoil is a very familiar airfoil that is commonly used for CFD prediction methods validation studies and also as the starting airfoil for many design optimization studies.

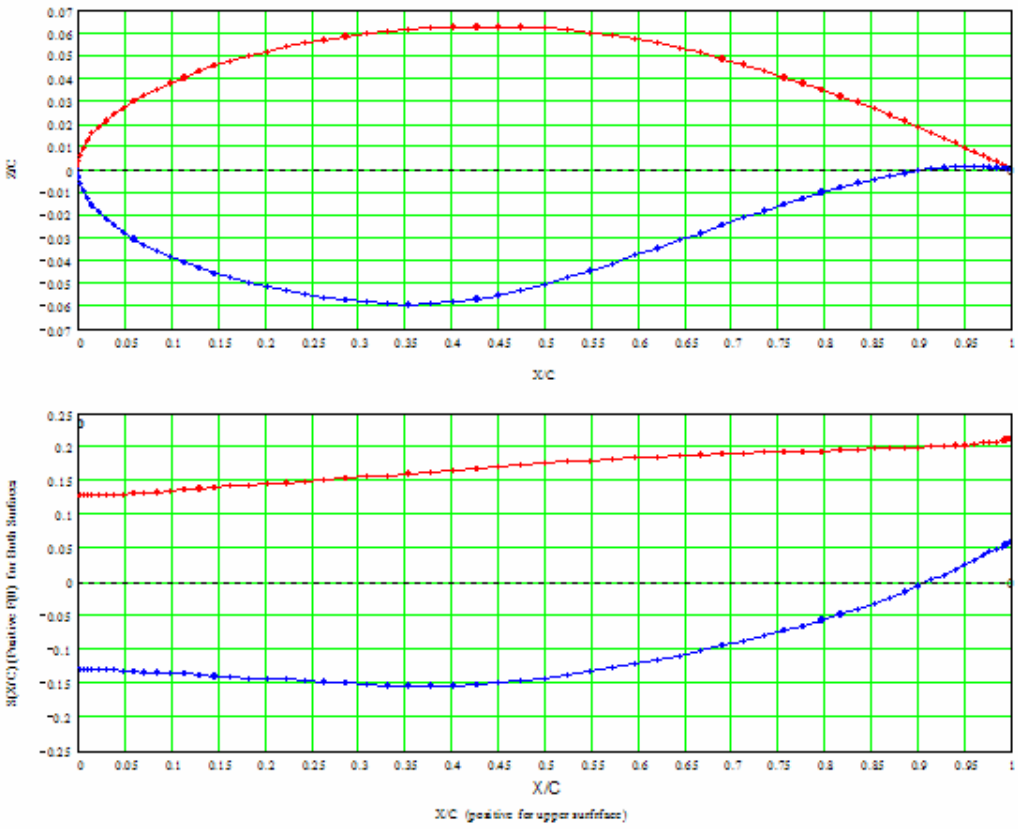

Figure 22. RAE 2822 Airfoil Geometry – (Defined by 130 "X, Z" Coordinates)

The convergence studies for the RAE2822 airfoil included very detailed comparisons of the geometric and aerodynamic characteristics of the RAE2822 airfoil with those calculated for 14 approximate airfoils obtained with BPO = 2 to BPO = 15 shape functions. The convergence of the upper and lower surfaces analytic shape functions with the RAE 2822 numerical shape functions with increasing BPO is shown in fig. 23. Negative values of lower surface shape functions are shown since this clearly demonstrates the match of lower surface and upper surface leading edge radii.

In this example, the upper surface converged slightly faster than the lower surface. For BPO8 and all higher PBO the analytic and numerical shape functions were found to be essentially identical on the upper surface, and also on the lower surface.

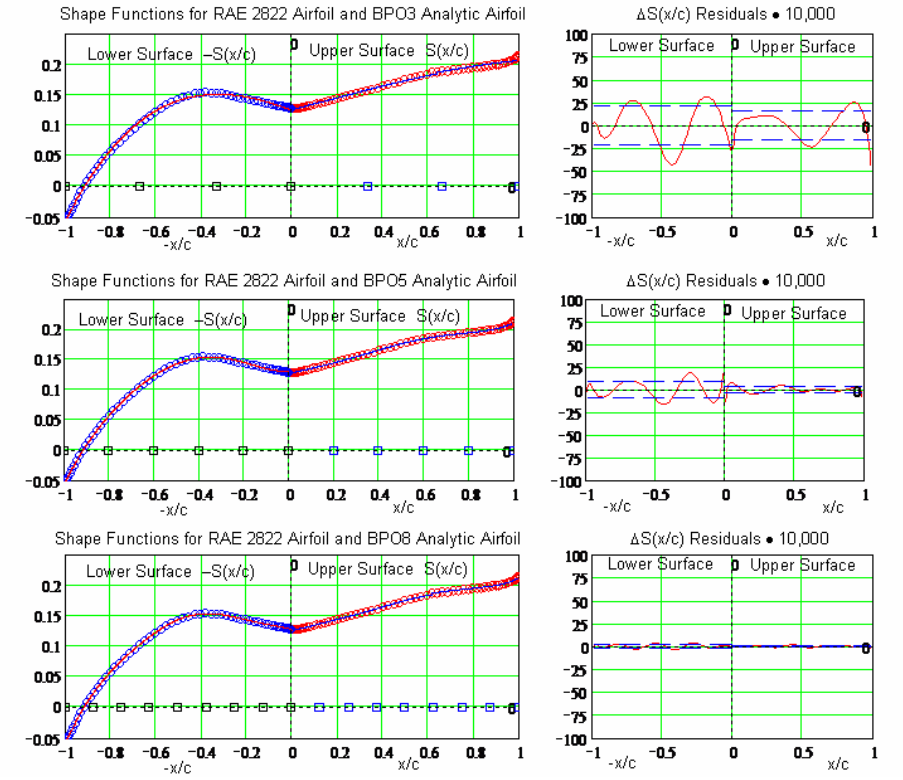

Figure 23. RAE2822 Shape Function Convergence Study

The convergence of the approximate upper surface and lower surface geometries, with the RAE 2822 numerical definition, as shown in fig. 24, is similar to the rapid convergence of the shape function with increasing BPO. The residual differences between the actual coordinates and the corresponding approximate geometry are also shown in fig. 24 along with the typical wind tunnel model tolerances.

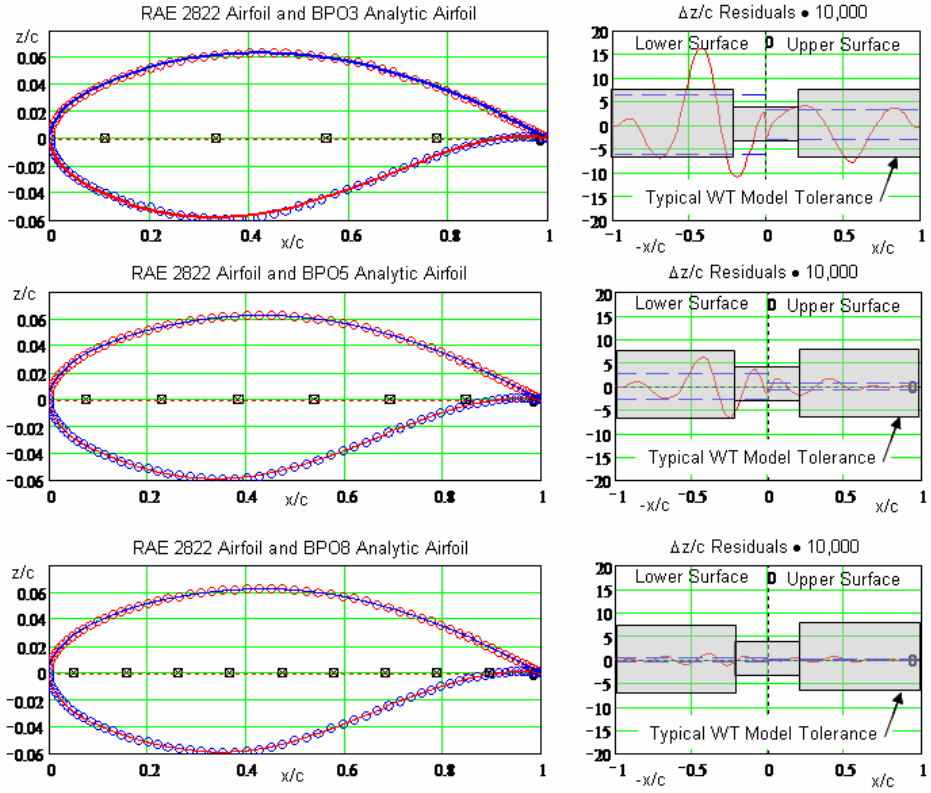

Figure 24. RAE2822 Airfoil Shape Convergence Study

The slopes, transformed slopes, 2nd derivatives and transformed 2nd derivatives for the analytical approximations of the RAE 2822 are compared with the corresponding values determined from the numerical definition of the RAE 2822 in fig. 25.

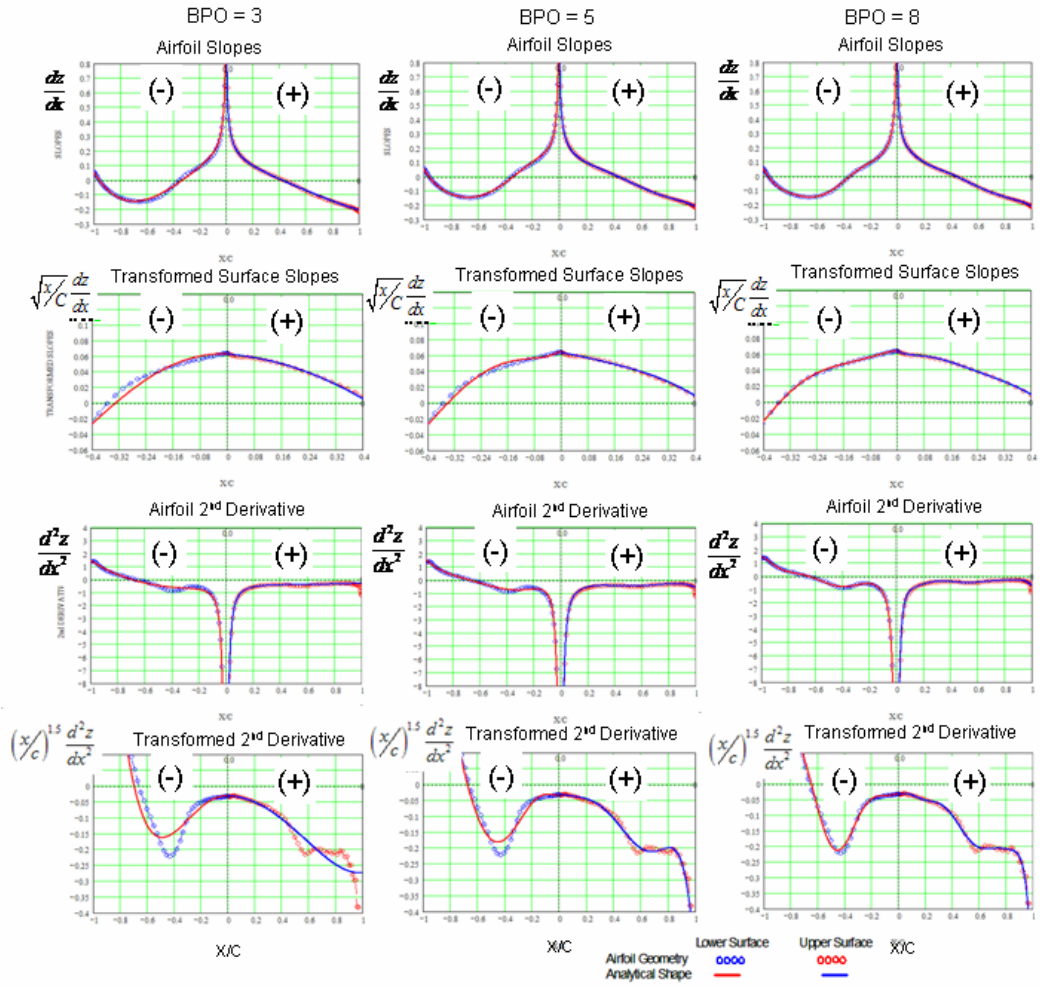

Figure 25. RAE2822 Airfoil Slope and 2nd Derivatives Convergence

Negative values of the slopes and 2nd derivatives are shown for the lower surface to provide a clearer illustration of the differences of the upper and lower surface geometry characteristics.

The transformed values of the slopes and of the 2nd derivatives allow the differences between values determined for the analytically defined airfoils and those determined from the official numerical definition of the RAE 2822 to be easily seen. The analytical slopes and 2nd derivatives of the analytical rapidly converge to match the corresponding values determined from the numerical airfoil definition.

Although not shown in the figure, as the BPO continues to increase, the differences in even the finest details between the airfoil characteristics determined from the analytical representations and the actual airfoil geometry continued to vanish.

The results of the statistical analyses of the quality of the agreement between the analytical airfoils and the numeric definitions are shown in the fig. 26. The results show that for BPO of about 6 and greater that the analytically defined airfoils indeed become statistically identical.

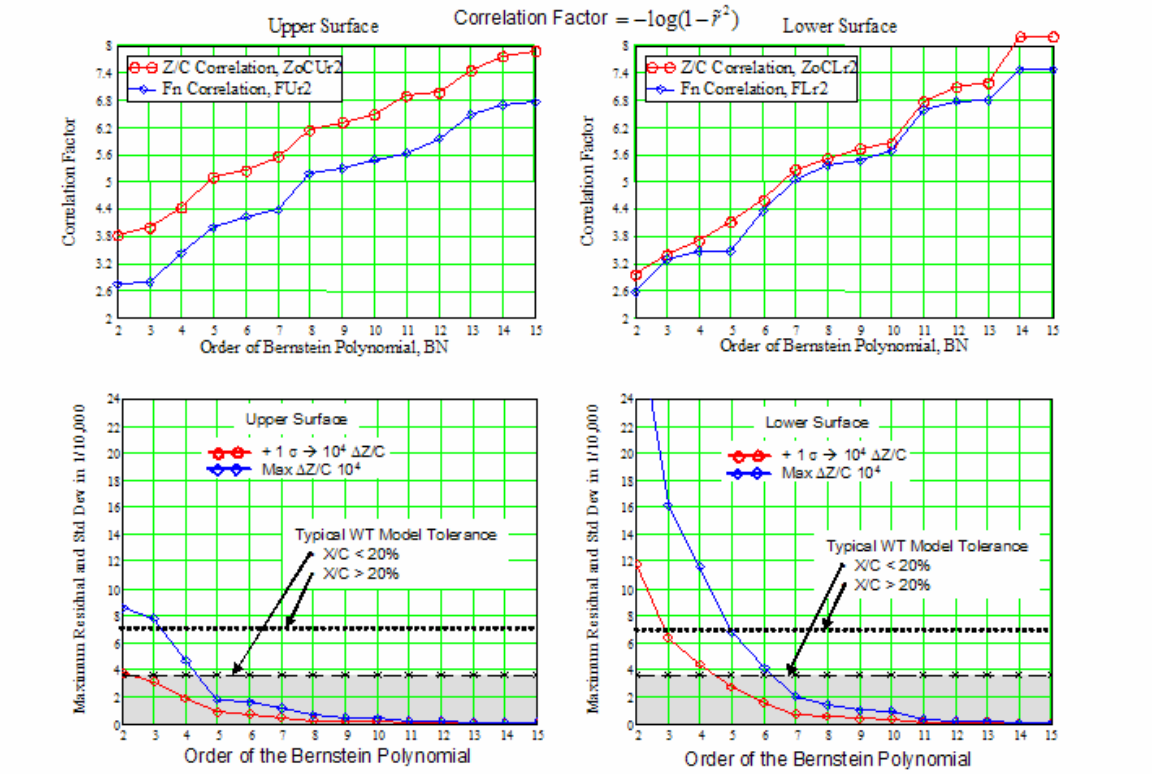

Figure 26. RAE2822 Airfoil Statistical Convergence

These results and those shown in the previous figure, show that the airfoils defined by BP representations of the shape functions by can match even the most intricate geometric characteristics of an airfoil.

The slopes, 2nd derivatives and curvature for the airfoil surfaces, and those for the corresponding shape functions used to define the analytical airfoils are compared in fig. 27.

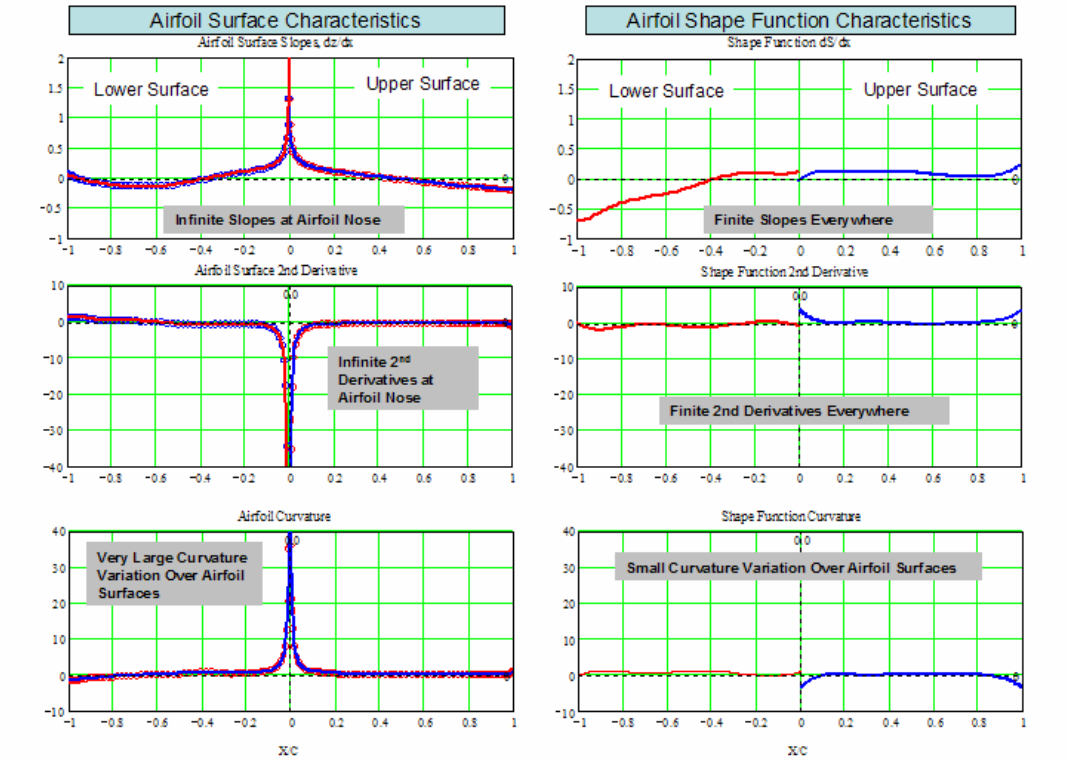

Figure 27. Mathematical Simplicity of the Shape Function – RAE 2822

Again, it is seen that the values of these quantities for the shape function are everywhere finite and vary by only small amounts over the airfoil surfaces. This once again demonstrates the mathematical simplicity and elegance of the shape function / class function methodology introduced in this report.

As a prelude to computing the pressure distributions and aerodynamic forces for baseline airfoils and shape function/class function analytical airfoils, a comparison was made of experimental pressure data for the RAE 2822 airfoil and predictions obtained with the TRANAIR full potential code with momentum integral coupled boundary layer. The objective was to demonstrate the well recognized prediction capability of the TRANAIR code. The results are shown in fig. 28 along with comparable predictions obtained with the WIND and NPARC Navier Stokes codes.

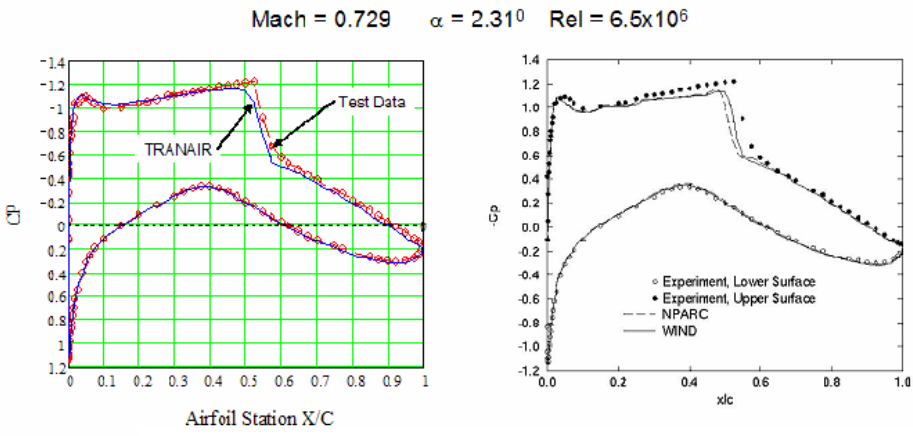

Figure 28. RAE 2822 Airfoil Test vs TRANAIR CFD Predictions

The TRANAIR predictions are in reasonably good agreement with the test data and appear to have even slightly better agreement with the test data than the corresponding Navier Stokes predictions.

Calculations were made of the pressure distributions for the numerically defined RAE 2822 and for a series of shape function derived analytical airfoils with BPO2 to BPO15 shape function definitions.

In all cases the defining inputs stations for the TRANAIR analyses were identical to the official defining stations for the RAE 2822.

Some of the results from these RAE 2822 analyses are shown in fig. 29 for a series of analytical representations corresponding to PBO2, BPO4, BPO6 and BPO8 “shape function” defined airfoils.

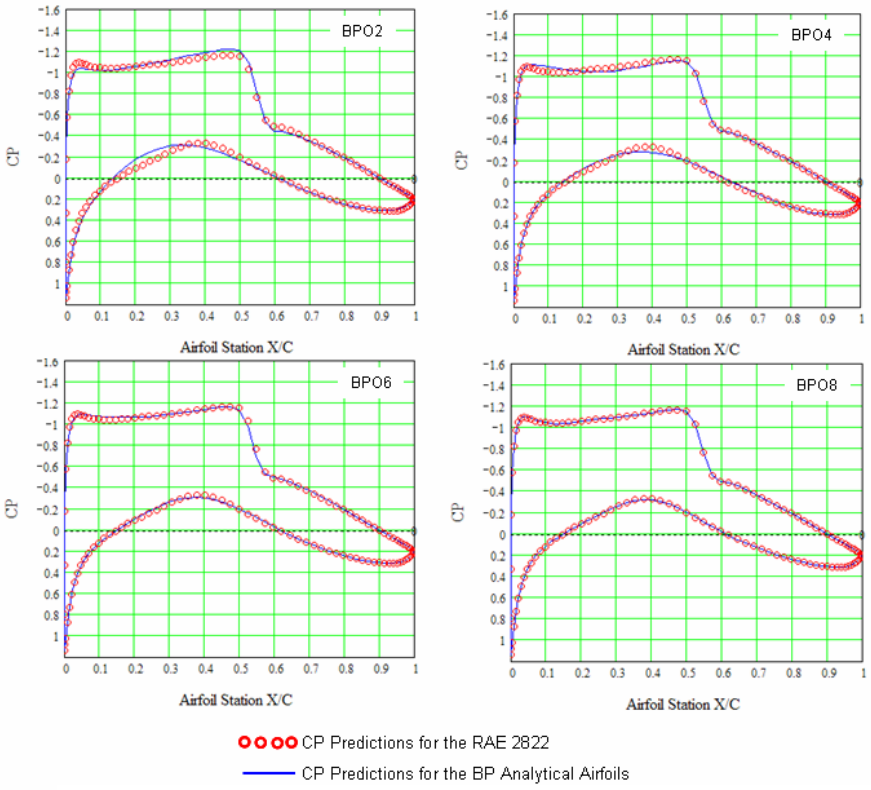

Figure 29: RAE2822 Pressure Distribution Convergence

The predictions of the BPO6 and BPO8 analytic airfoils closely match the upper surface pressure distributions for the numerically defined airfoil. The pressure distribution for even the BPO2 representation, which is defined by only 6 variables for representing both the upper and lower surfaces of the airfoil, appear to be quite close to the actual airfoil upper surface pressure distribution.

The two lowest order BP airfoils, have very slight differences in the lower surface CPs from those of the numerically defined airfoil. The upper and lower Cp distributions for all the BPO6 and above airfoils appeared to exactly match those for the RAE 2822 numerical definition.

Comparisons of the lift and drag predictions are shown in fig. 30.

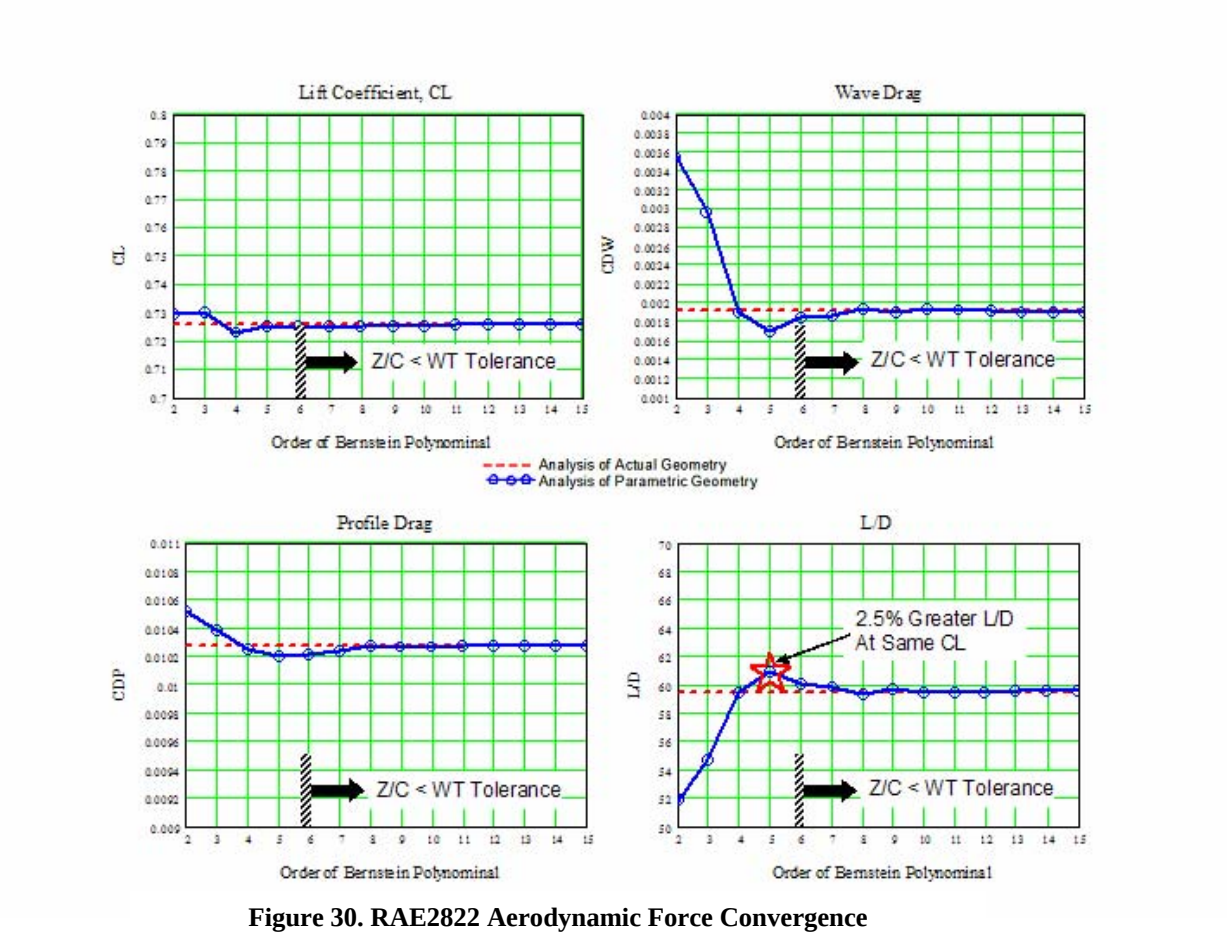

Figure 30. RAE2822 Aerodynamic Force Convergence

The lift predictions for all BPO5 and greater airfoils matched the RAE 2822 predictions. The drag predictions for BPO8 and above agree exactly with the predictions for the actual RAE 2822. Both the profile drag and wave drag for the BPO5 airfoil are less than that of the baseline RAE 2822 airfoil even though the lift predictions are identical. Consequently the least squares shape function matching study which was certainly not intended as a design optimization study, did result in an airfoil geometry with a 2.5% increase in lift/drag ratio over that of the RAE 2282 airfoil. This is most likely the result of the smoothing capability inherent in the class function / shape function methodology.

Comparisons of predicted pressure distributions for the actual RAE 2822 airfoil and the BPO8 airfoil are shown in fig. 31 for a series of Mach numbers and for zero angle of attack. The BPO8 pressure distributions all match those obtained with the actual RAE 2822 airfoil geometry.

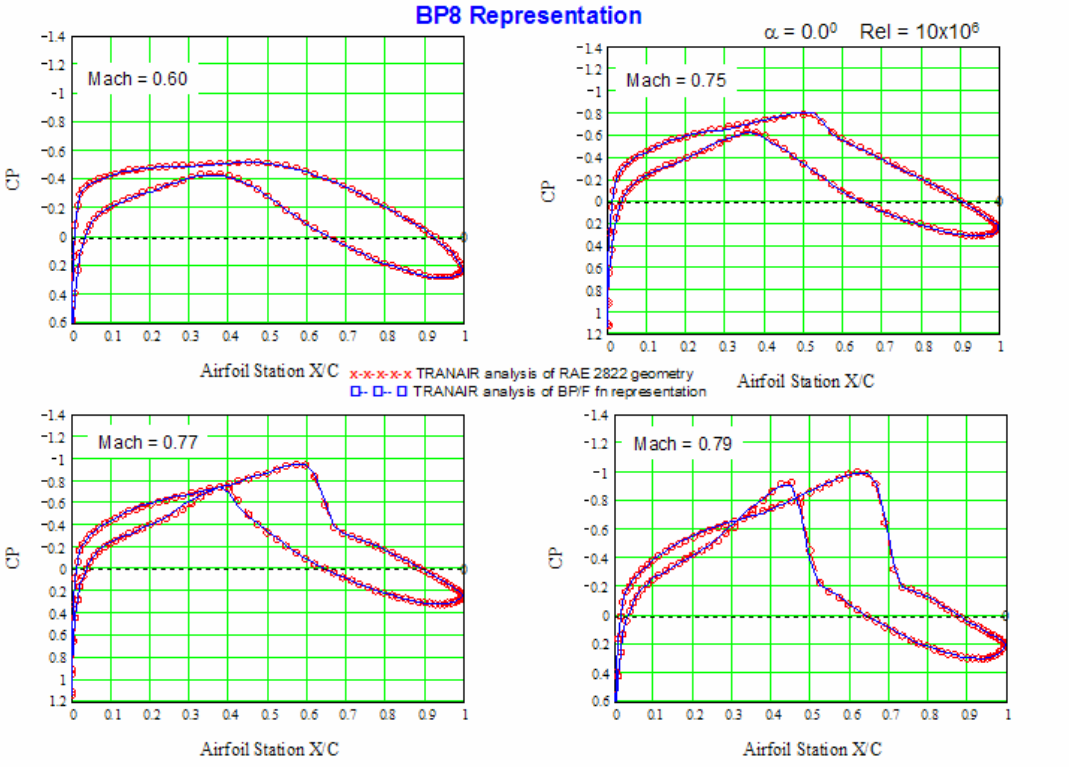

Figure 31. RAE2822 Pressure Distribution Comparisons - BPO8, α = 0.0 deg

Similar CP predictions are shown at an increased angle of attack of 2.31 degrees for a range of Mach numbers up to and beyond the drag divergence Mach number in fig. 32. Again the agreement between the BPO8 analyses and the RAE 2822 airfoil analyses are excellent.

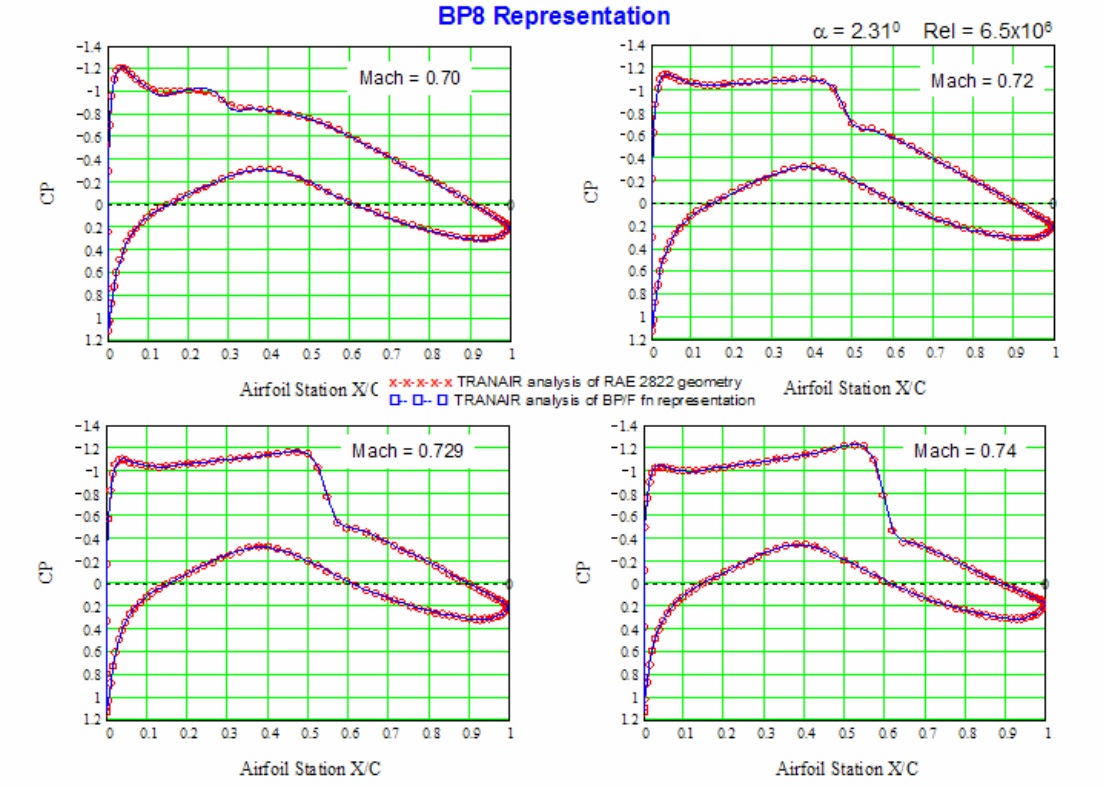

Figure 32. RAE2822 Pressure Distribution Comparisons BPO8, α = 2.31 deg

The results of the lift, drag and pitching moment predictions for both zero angle of attack and an angle of attack of 2.31 degrees are shown in fig. 33 for the BPO8 airfoil and the actual RAE 2822 airfoil definition. The force predictions for the BPO8 airfoil exactly match those of the RAE 2822.

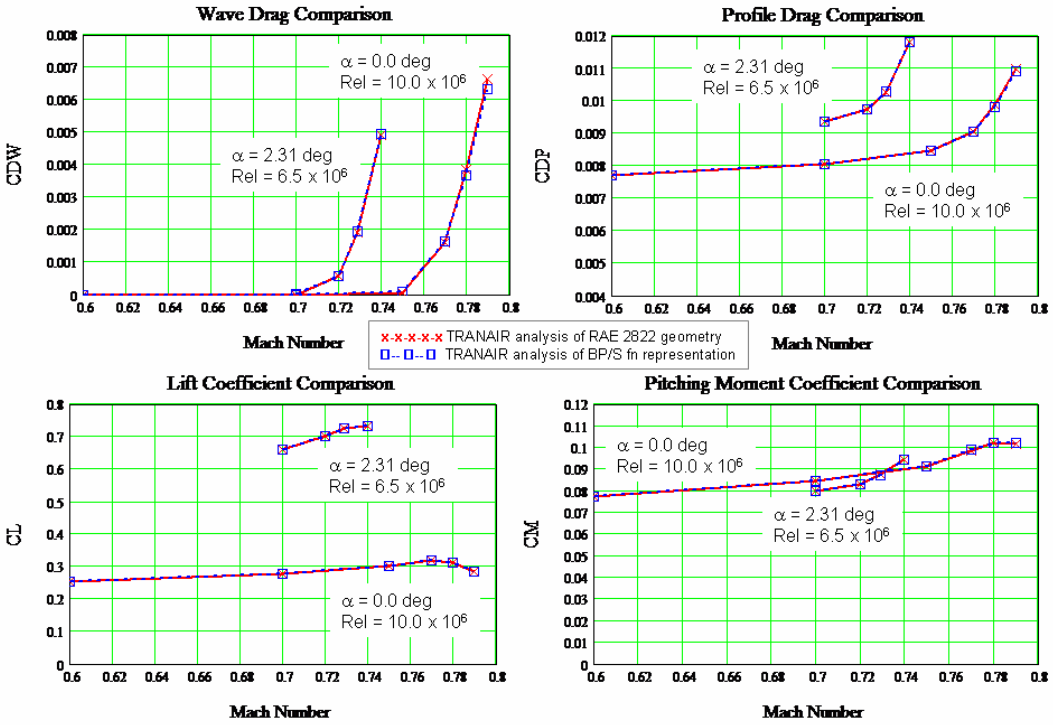

Figure 33. RAE2822 Aerodynamic Force Comparisons BPO8

The results of the CP and force comparisons that have been shown, along with the previously discussed geometric comparisons, imply that a relativity low order BP shape function airfoil with only a relatively small number of variables can represent a supercritical type airfoil.

D. NASA Supercritical Airfoil NSC 2-0714 Study

The NASA supercritical airfoil NSC 2-0714 is another of the many airfoils that have been used to help establish the effectiveness of utilizing the shape function / Bernstein polynomial airfoil representation methodology. This airfoil as defined by a total of 142 "x,z" vector pairs is shown in fig. 34 along with the corresponding shape functions for the upper and lower surfaces computed from the actual airfoil defining coordinates. This is an example of an airfoil that has a finite trailing edge thickness.

Comparison were made of the defined geometry, and calculated aerodynamic characteristics of the NASA NSC 2-0714 airfoil, with the corresponding results of 14 different approximating airfoils with shape functions, determined for various orders BP (from BPO = 2 to BPO = 15) by the least squares fitting process.

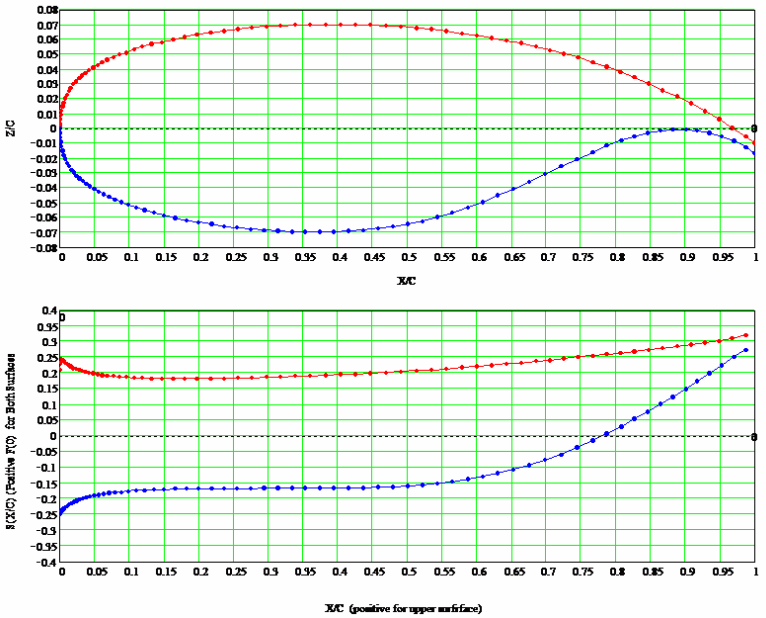

Figure 34. NASA Supercritical Airfoil (NSC 2-0714) Geometry

Some of the geometric comparison results are shown in figs 35 through fig. 37. Examples of the shape function comparisons are shown in fig. 35.

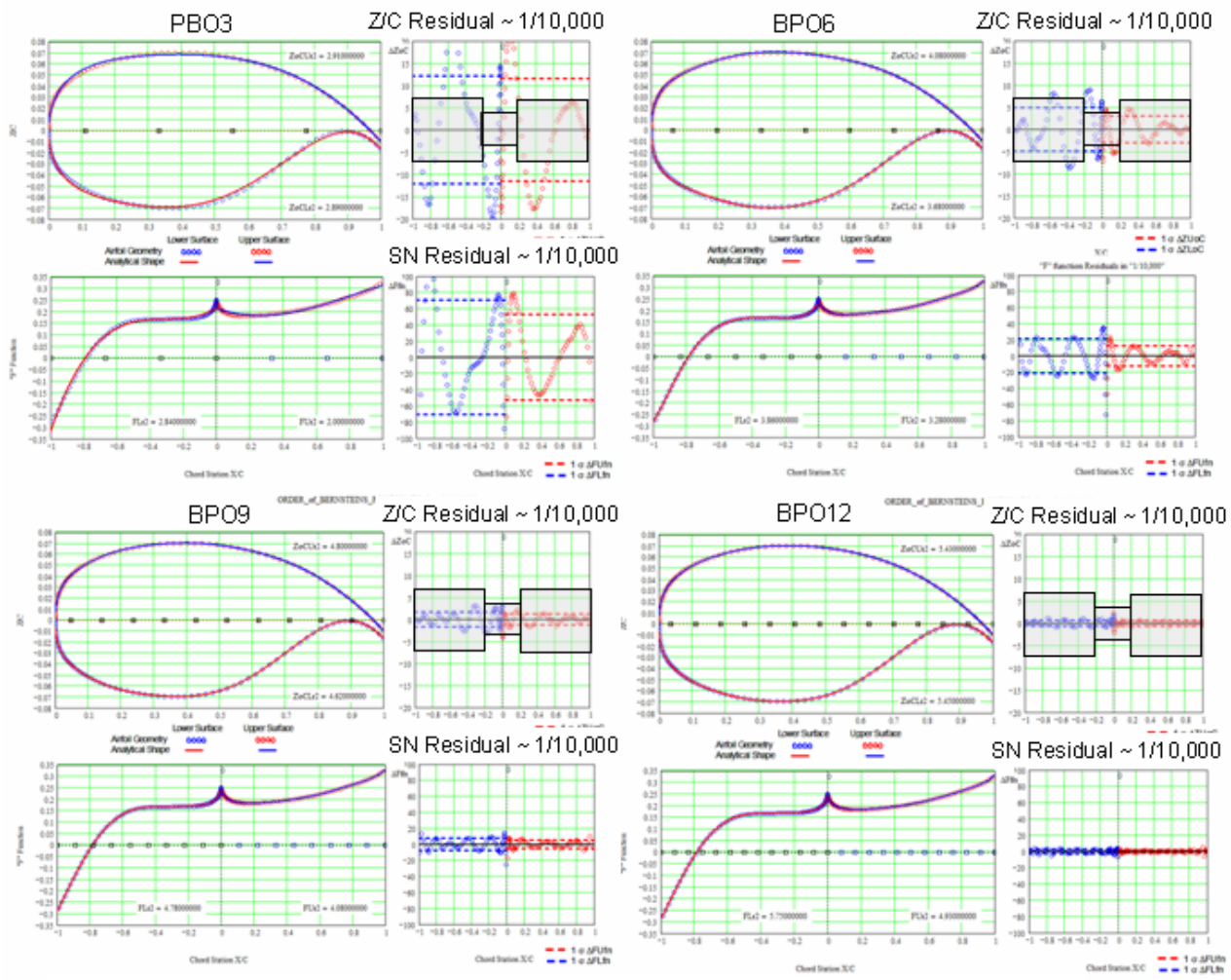

Figure 35. NASA Supercritical Airfoil (NSC 2-0714) Geometry Convergence Study

The residual differences between the shape functions are also shown together with the overall 1 sigma standard deviations. Even the lowest PBO shape functions, which represented each surface by only 4 variables, appear to closely match the actual airfoil shape functions. The corresponding approximating airfoils surface coordinates, as expected, also closely matched the actual airfoil geometry. As the BPO increases the residual differences once again vanish, leading to essentially exact geometric matches.

The slopes, transformed slopes, 2nd derivatives and transformed 2nd derivatives corresponding to the various approximating airfoils, are compared with the corresponding actual airfoil data in fig. 36. It is seen that even the lowest order BPO3 slopes and 2nd derivatives capture the basic characteristics of the airfoil slopes and 2nd derivatives. This is further testimony to the power inherent in the BP shape function airfoil geometry representation process.

As the BPO is increased from 3 to 15, the approximating airfoils capture even the most intricate details of the slope and 2nd derivative curves. The 2nd derivatives for the actual airfoil show a significant amount of jagged irregularities and yet the shape function defined airfoils smooth out all of the irregularities.

The shape function geometries are seen to result very smooth airfoil shapes. The BP shape function airfoil methodology consequently, can be used to smooth any airfoil definition

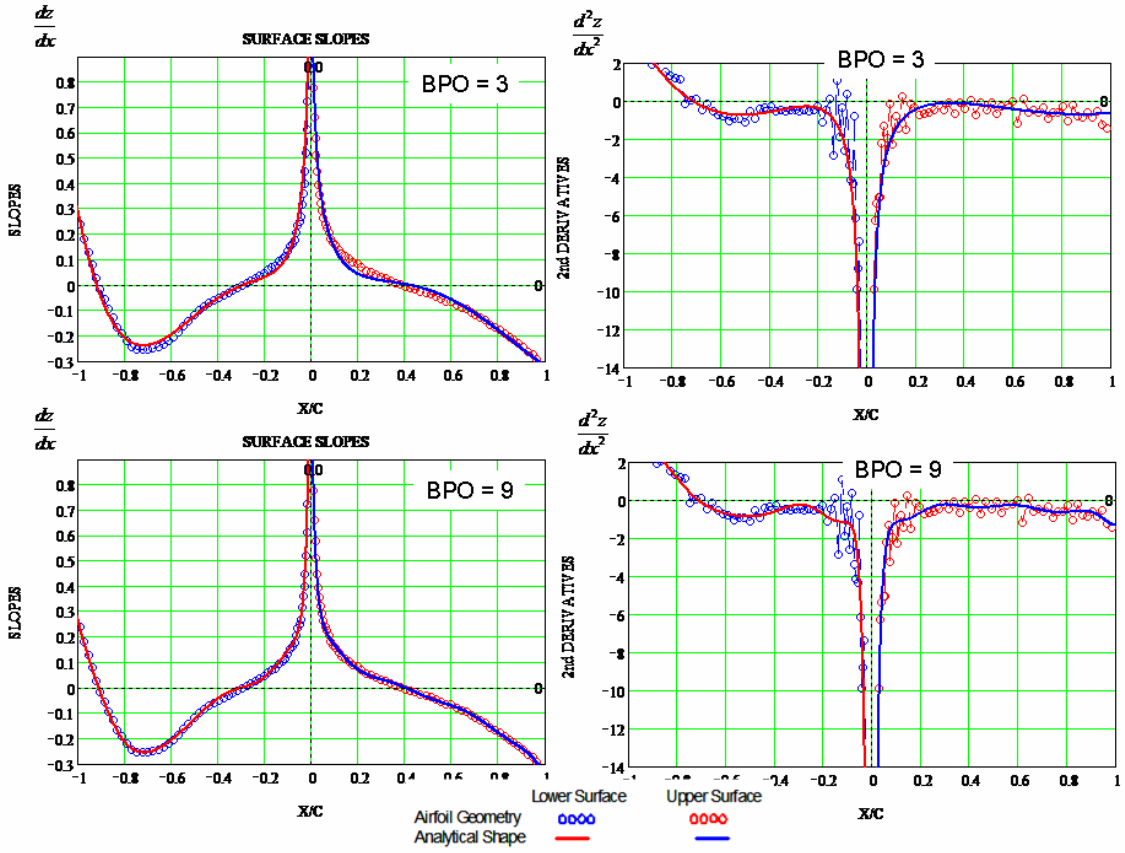

Figure 36. NASA Supercritical Airfoil (NSC 2-0714) Slopes and 2nd Derivatives Convergence Study

The results of the statistical analyses of the geometric convergence with increasing BPO are shown in fig. 37. As is the case with the previously shown other airfoil data, the statistical convergence of the PB airfoils with increasing BPO is quite uniform and rapid. The BPO = 8 and above approximate airfoil geometries match the actual airfoil geometry within wind tunnel model tolerances.

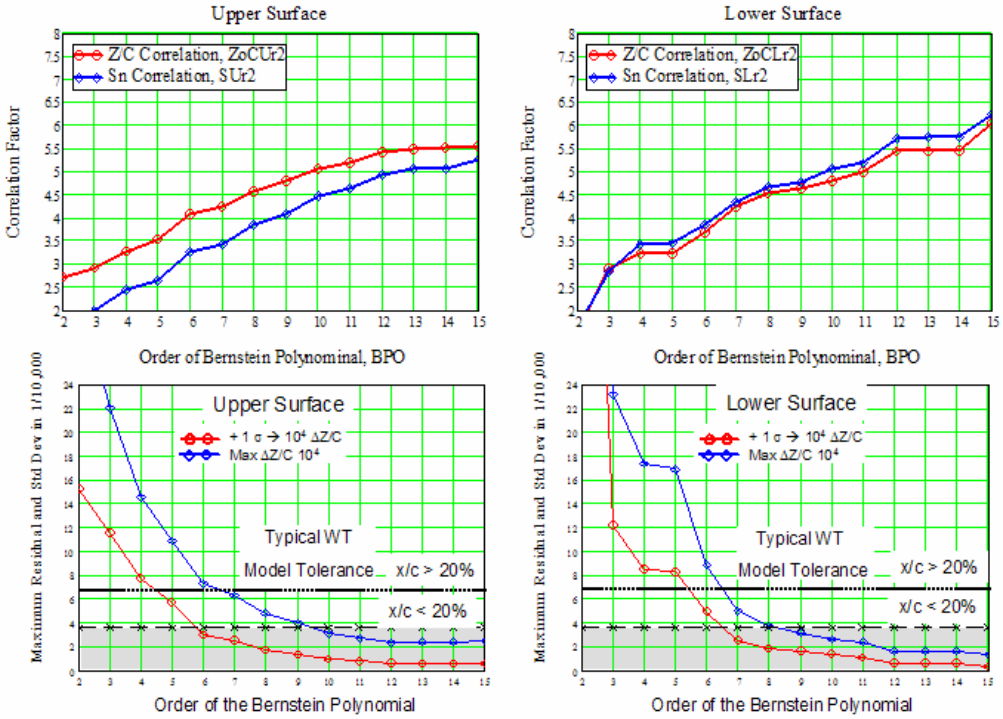

Figure 37. NASA Supercritical Airfoil (NSC 2-0714) Statistical Convergence Study

Calculations were also made with the TRANAIR full potential plus boundary layer CFD code of the pressure distribution for the NSC 2-0714 airfoil, and for the family of least squares fit BP shape function defined airfoils with BPO2 to BPO15. Some of the results are shown in the fig. 38. The pressure distributions for the all BP airfoils capture the upper surface shock strength and location. The BPO10 airfoil pressure distribution exactly matches that of the actual airfoil.

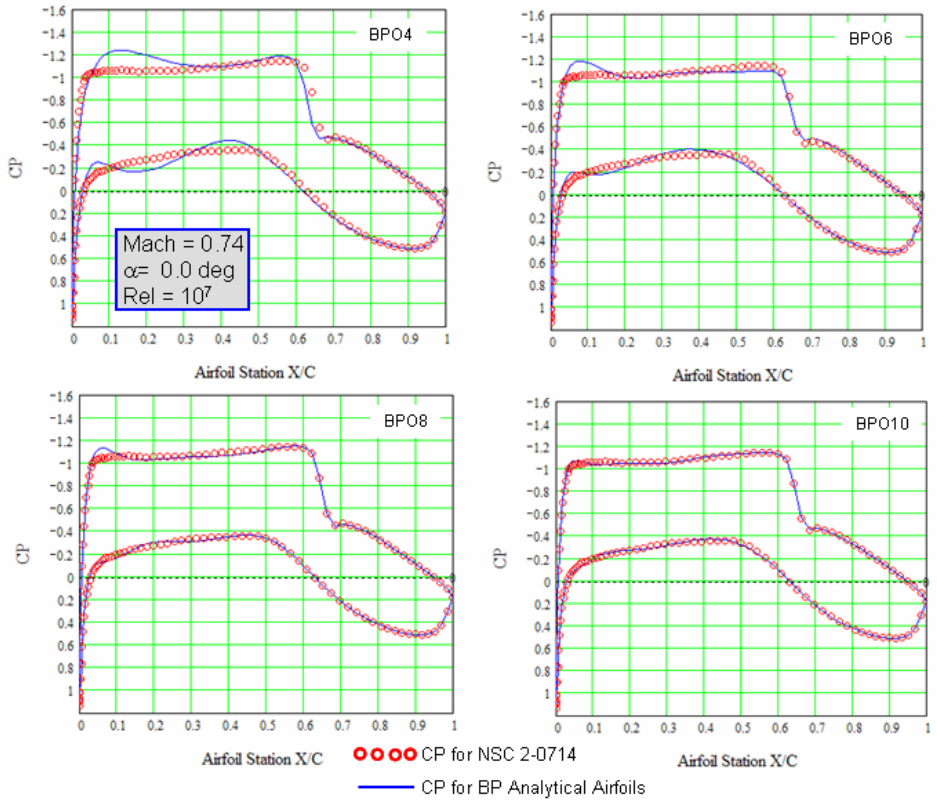

Figure 38. NASA Supercritical Airfoil (NSC 2-0714) Cp Convergence Study

Results of the lift, wave drag, profile drag and lift/drag ratio comparisons are shown in the fig. 39.

The aerodynamic forces for BP10 and above airfoils, exactly match the values for the calculated for actual airfoil. The PBO4 to PBO7 airfoils, which, as previously shown, closely match the actual airfoil geometry, all achieved at least a 5% greater L/D that of the actual optimized airfoil.

Although the current study was a “matching” rather than design optimization study, it did result in an improved aerodynamic design.

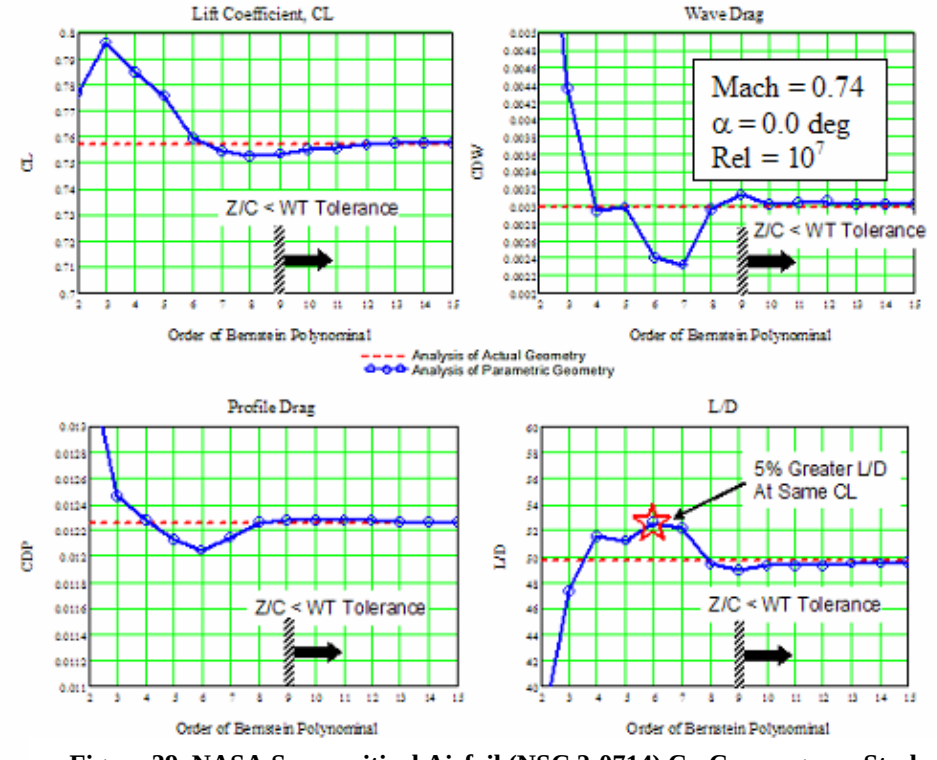

Figure 39. NASA Supercritical Airfoil (NSC 2-0714) Cp Convergence Study

The comparison wave drag values in fig. 39, are above the level commonly used to define the critical Mach number. Typically, critical Mach number for an airfoil is associated with a wave drag level of CDW $\approx$ = 0.0020.

The wave drag increases rapidly with further increases in Mach number. The wave drag for Mach numbers beyond the critical Mach number, are typically sensitive to relatively small geometry changes. This may explain the seemly large change in drag corresponding to very small changes in airfoil geometry between the various BP airfoils.

Pressure distributions calculated for the BPO8 approximate airfoil are compared with the corresponding pressure distributions for the actual airfoil geometry in the fig. 40 for a series of Mach numbers. The agreement between the pressure distributions of the two airfoils is seen to be very good for all of the Mach numbers.

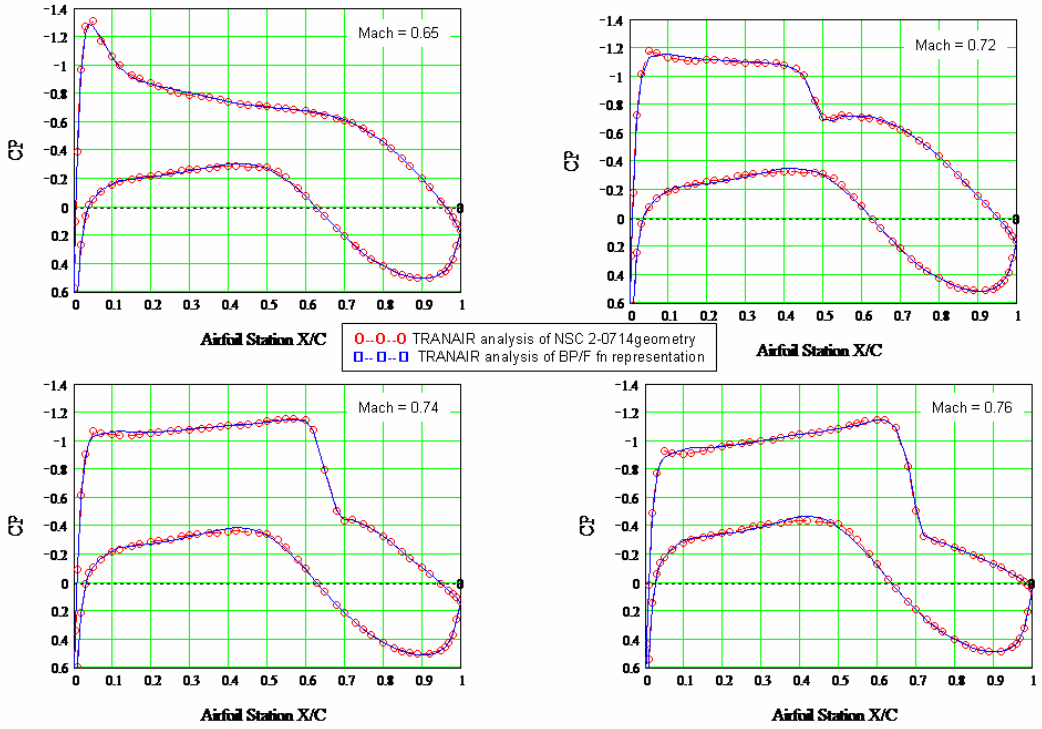

Figure 40. NASA Supercritical Airfoil (NCS 2-0714) CP Comparisons

The corresponding lift and drag predictions for the two airfoils are shown in the fig. 41. It is seen that the force predictions obtained with the BPO8 airfoil matches the corresponding aerodynamic forces and drag rise characteristics of the actual airfoil across the entire Mach range.

The results, that have been shown for the three example airfoil studies in this report, are typical of the results obtained for all the other airfoils that have been studied to date.

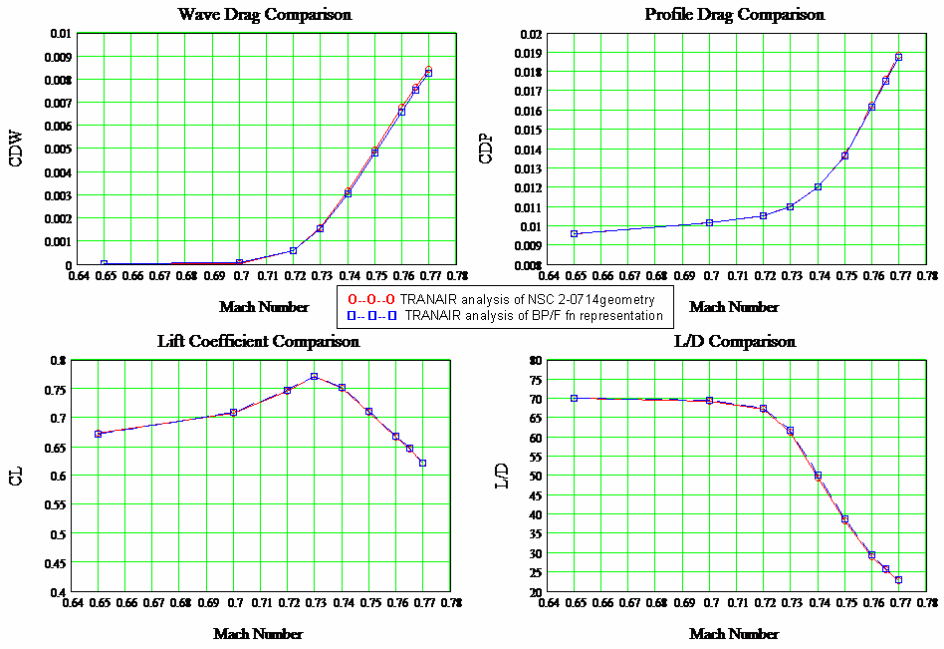

Figure 41. NASA Supercritical Airfoil (NSC 2-0714) Force Comparisons

E. Potential Design Applications

The results of the detailed airfoil comparison studies show that a relatively low order Bernstein polynomial, (typically BPO6 to BPO9), matched the airfoil geometry and the aerodynamic forces. The results also have shown that lower order BP representations still closely match the existing airfoil geometry and typically improved the aerodynamic performance even though as previously mentioned the reported studies did not involve design optimization. This suggests that even lower order Bernstein polynomials, corresponding to fewer design variables, (perhaps BPO4 to BPO6), could produce optimum designs.

In any case, however, this methodology does offer a systematic option for a systematic approach for design optimization. The optimization process could initially be conducted with a low order BP for the shape function to obtain an optimum design. The order of the BP could then be increased and the conduct another optimization to determine if a better optimum design is achieved. As previously shown (fig. 13), the peaks of the basis shape function are uniformly distributed along the chord of the airfoil. Hence increasing the order of the BP used to represent the shape functions, provides a systematic way to uniformly increase the number of design variables.

In the previously discussed studies, the PB shape function airfoil definitions used the same order BP for both the upper and lower surfaces. Although this is not a requirement, it does provide a very convent means for determining the component camber and thickness distributions for an airfoil by simply adding and subtracting the unit shape function scaling coefficients as shown in the fig. 42.

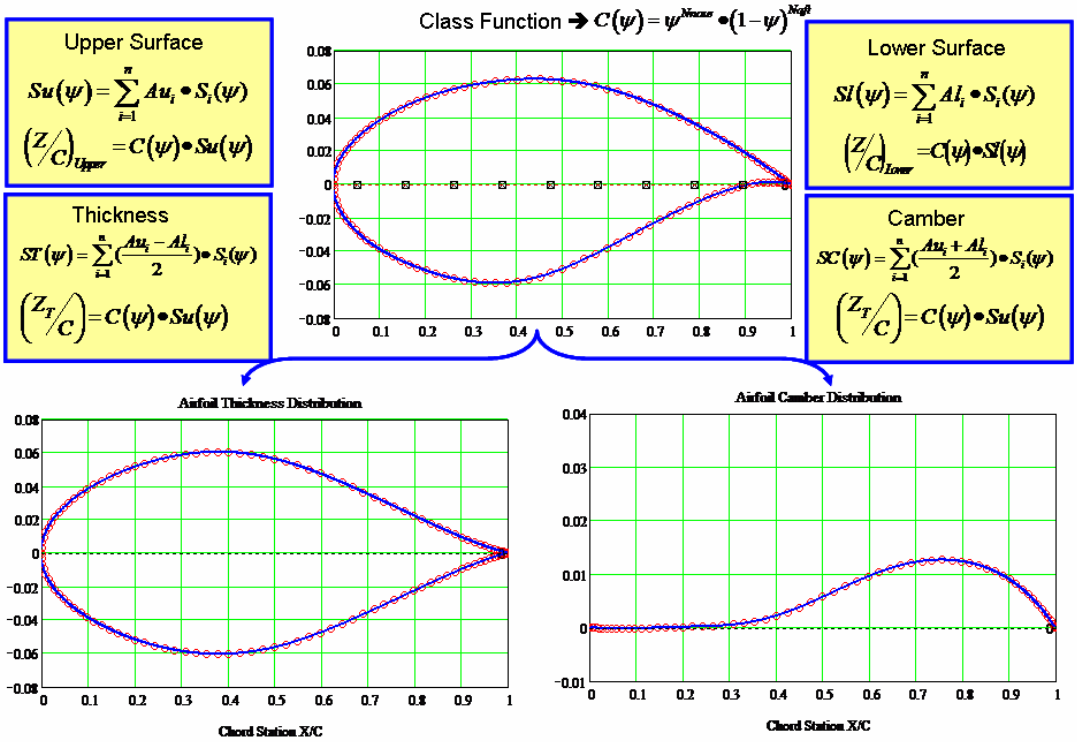

Figure 42. Simple Decomposition of an Airfoil into Thickness + Camber

This also provides a number of convenient options for using the BP shape function airfoil representations for airfoil design optimization applications. These include:

1. Optimization with both the upper and lower surface BPO scaling factors as the design variables.
2. A desirable design option provided by this methodology can insure equal leading radii on the upper surface and on the lower surface and therefore, continuity of curvature around the leading edge of the airfoil. This is easily achieved by requiring the first BP coefficient of the upper surface to match the first BP coefficient of the lower surface.

3. Any airfoil geometry can be selected as the baseline airfoil for the optimization process. The baseline airfoil can be represented by as a BP shape function airfoil using the previously discussed least squares fit process. The resulting PB coefficients can be used as initial values for the design process.
4. The BP shape function coefficients for a baseline airfoil can be decomposed into a set of thickness coefficients and a set of camber coefficients. The thickness coefficients can be held constant and the camber coefficients can be selected as the design variables. Conversely, the camber coefficients can be held constant and the thickness coefficients can be selected as the design variables. In either case the airfoil upper surface and lower surface of the airfoil are easily defined by adding or subtracting the thickness and camber coefficients.
5. The leading edge radius radii can be defined and held constant by assigning a value for the first coefficients of the upper surface BP and lower surface BP.
6. The trailing edge boattail angle on the upper surface and / or on the lower surface can be held constant by specifying the last term in the respective BP.
7. The airfoil closure thickness can be set by the definition of the shape function.

The previously discussed studies were focused on 2D wing type shapes with round leading edges and finite slope trailing edges corresponding to a class function with coefficients N1 = 0.5 and N2 =1.0. The results and conclusions of these studies apply equally well to other classes of geometries such as those shown in the fig. 43. The results and conclusions will also apply to axi-symmetric nacelles and to bodies of revolution.

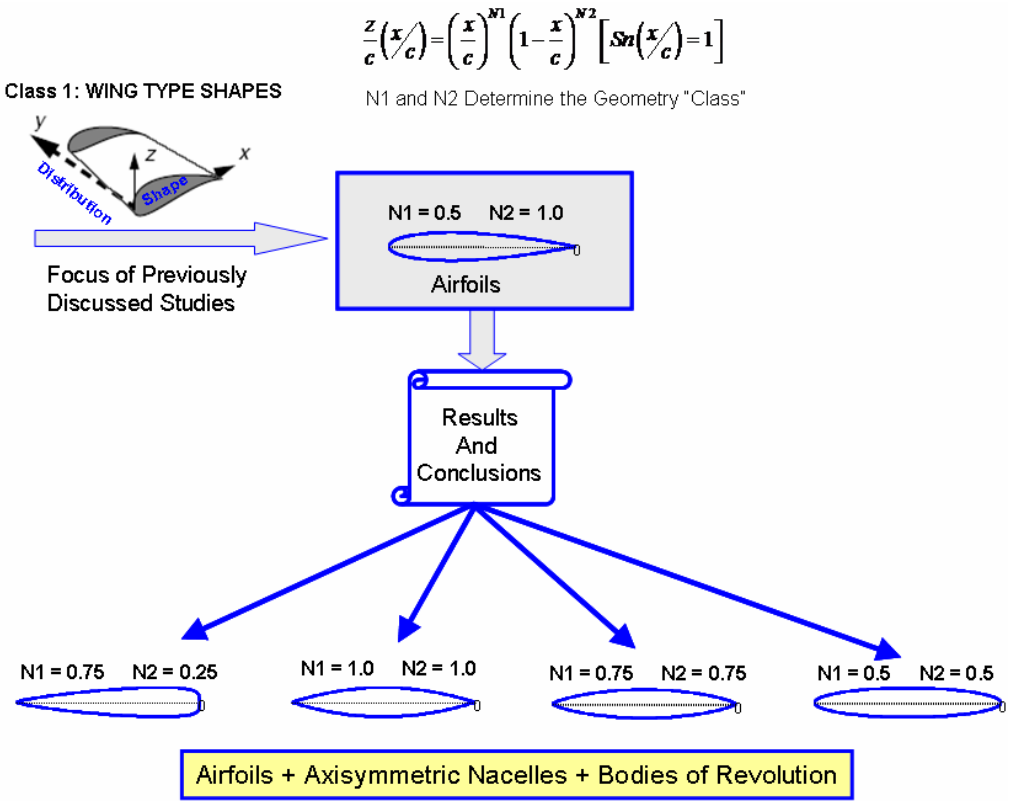

Figure 43. Extension of Previous Studies Results

VI. Extension to 3D Geometries

The shape function / class function methodology of representing a 2D geometry will now be shown to be applicable for representing the cross sectional shapes of the class 2 aerodynamic components which are the "body type" geometries. In many cases, the methodology can also be used to define the distribution of the shapes along the body axis thereby defining the geometry of complete three dimensional shapes.

The shape function / class function methodology can be used to describe the geometry of the upper or lower lobe cross-section -of a body. Let us assume initially that a body cross-section is laterally symmetric and has the shape of an ellipse as shown in fig. 44. We will then subsequently generalize the results using the class function.

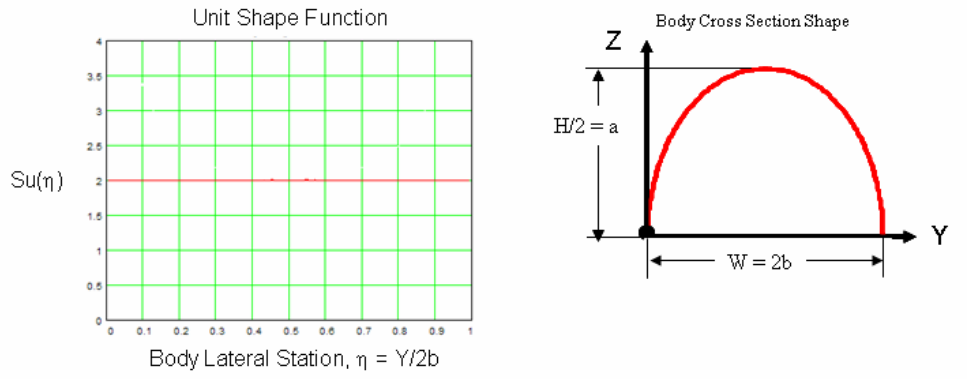

Figure 44. Representation of a Body Upper or Lower Lobe Shape

The equation for the ellipse with the axes of the ellipse at the left edge can be expressed as:

$$\zeta(\eta) = 2\eta^{0.5}(1-\eta)^{0.5} \tag{23}$$

Where: η = y/w and ζ = z/h

The shape function for this upper lobe elliptic geometry is therefore:

$$Su(\eta) = \frac{\zeta u(\eta)}{\eta^{NC1}(1-\eta)^{NC2}} = 2 \tag{24}$$

In the above equation we have generalized the definition of the class function by using the variable exponents NC1 and NC2

$$C(\eta)=\eta^{NC1}(1-\eta)^{NC2} \tag{25}$$

The cross section geometry equation expressed in terms of the shape function and the class function becomes:

$$z(\eta) = Su(\eta)\, C(\eta) \tag{26}$$

For an elliptic upper lobe shape, the shape function is a constant and equal to 2.0, and the class function exponents are: NC1 = NC2 = 0.5

Varying the exponent of the class function provide a simple technique to generate wide variety of body cross section shapes as shown in fig. 45. In these examples, the shape function is a constant value which is the unit shape function. By using the previously described Bernstein polynomial technique to represent the unit shape function together with the body cross-section aspect ratio of the body cross-section (ratio of body cross-section width to body cross-section height), a limitless variety of smooth cross-sectional geometries can be generated with just a few variables.

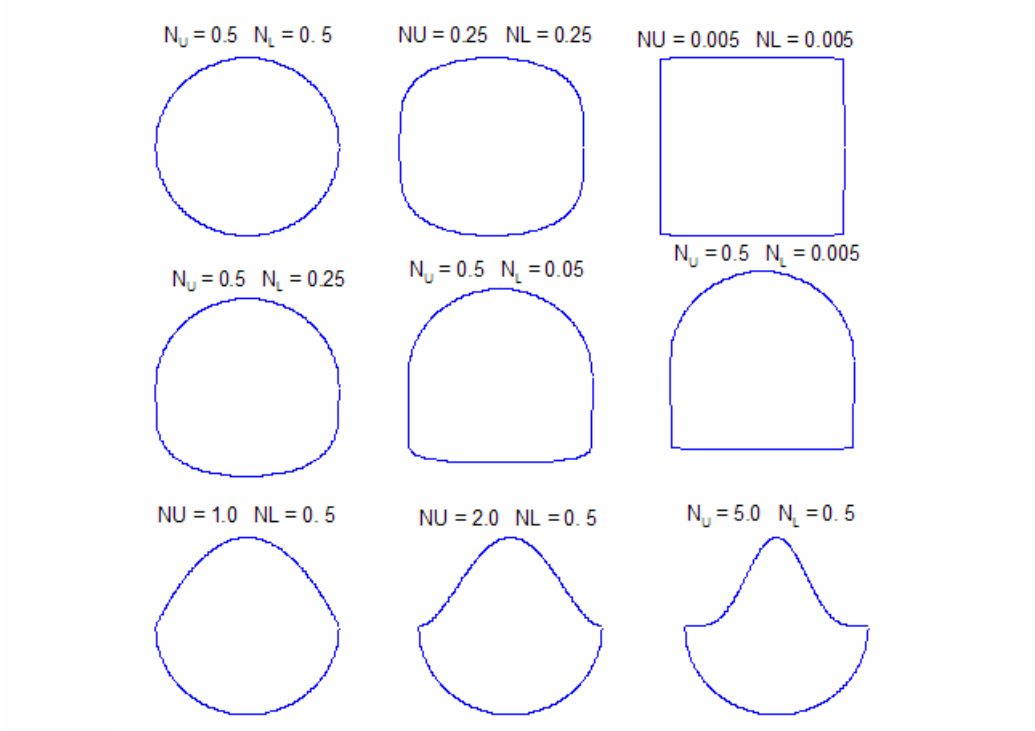

Figure 45. Examples of Body Upper or Lower Lobe Geometries

Another method to describe the cross sectional of a body is to use the shape function to describe one side of the cross-sectional shape of a body as shown in the fig. 46. The opposing side is then defined by the condition of lateral symmetry. The equations describing the geometry in this case are then:

$$\eta(\zeta) = 2\zeta^{0.5}(1-\zeta)^{0.5} \tag{27}$$

Where $\zeta = z/h$ and $\eta = 2y/w$

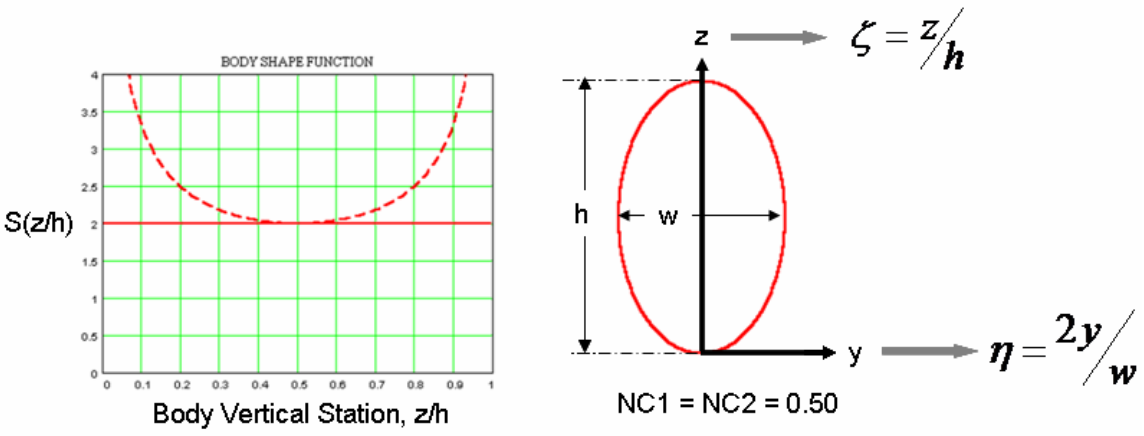

Figure 46. Representation of a Body Cross Section Right or Left Lobe Shape

Examples of cross-sectional shapes that can be obtained by simply varying the class function exponents are shown in fig. 47. Both of these methods to define body cross-sections can be used to develop rather general 3D geometries[13]. Some simple examples are shown in the subsequent sections of this report.

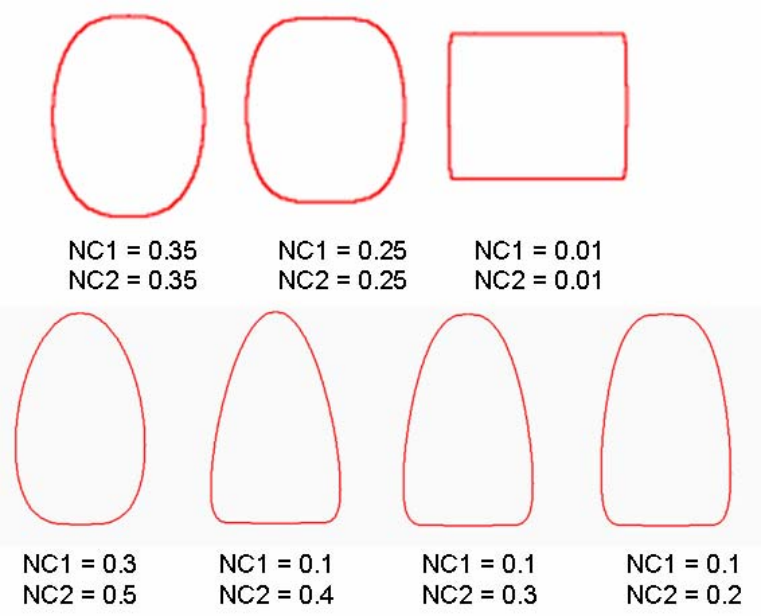

Figure 47. Various Body Cross-sectional shapes

A. <u>3D Bodies ➔ Distribution of Shapes</u>

Three dimensional geometries, as shown in fig. 48, can be considered to be a distribution of 2D cross-sectional shapes. In many instances, the distribution of the cross-section shapes along the generating axis, can also be described using the shape function / class function methodology.

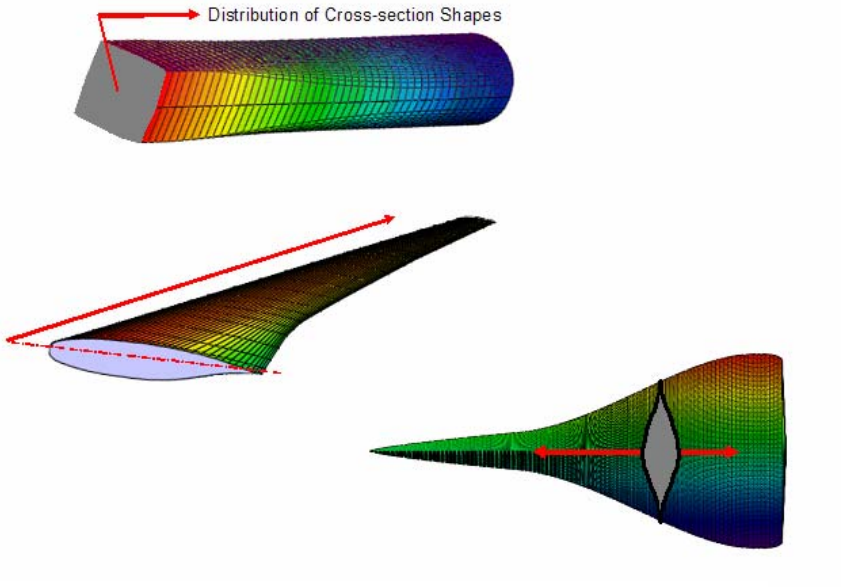

Figure 48. Examples of 3D Geometries as Distribution of Shapes

The concept of using the shape function / class function methodology to describe both the cross-sectional shapes and the distribution of the shapes is easily shown for the simple case of a cube in fig. 49.

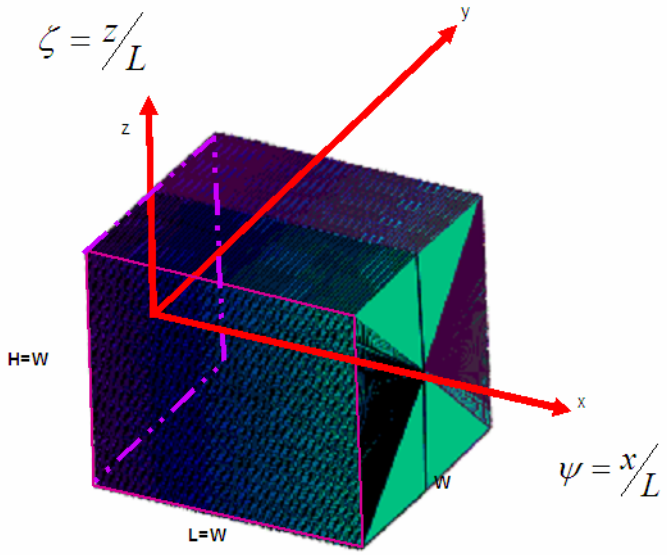

Figure 49. Definitions of Cross-section Shape and Shape Distributio n

The cross-section shape function, Sc, and class function, Cc, are defined by the equations:

$$Sc = 0.5^{2 \cdot NC} \tag{28}$$

$$C_c(\eta) = \eta^{NC}(1-\eta)^{NC} \qquad \eta \rightarrow 0 \text{ to } 1 \tag{29}$$

The distribution shape function, Sd, and class function, Cd, are defined by the similar equations;

$$Sd = 0.5^{2 \cdot ND} \tag{30}$$

$$Cd(\psi) = \psi^{ND}(1-\psi)^{ND} \qquad \psi \rightarrow 0 \text{ to } 1 \tag{31}$$

NC and ND are the class function exponents.

As shown in fig. 49: L = the body length, W = the body width, and H = the body height

The defining x, y and z coordinates are given by the equations:

$$x(\psi) = \psi \cdot L \tag{32}$$

$$y(\psi,\eta) = -\left[Sd \cdot Cd(\psi)\right] \cdot \left[1 - 2 \cdot \eta\right] \cdot \frac{W}{2} \tag{33}$$

$$z(\psi,\eta) = \pm\left[Sd \cdot Cd(\psi)\right] \cdot \left[Sc \cdot Cc(\eta)\right] \cdot \frac{H}{2} \tag{34}$$

For a simple unit cube: L = W = H =1 and NC = ND $\underline{\sim}$ 0.001

Examples of various geometries determined using equations 28 through 34, with various combinations of the class functions exponents, are shown in fig. 50. Notice that a value of ND = 0 results in an open flow through object, and a value of ND $\underline{\sim}$ 0.005 results in a similar but solid geometry.

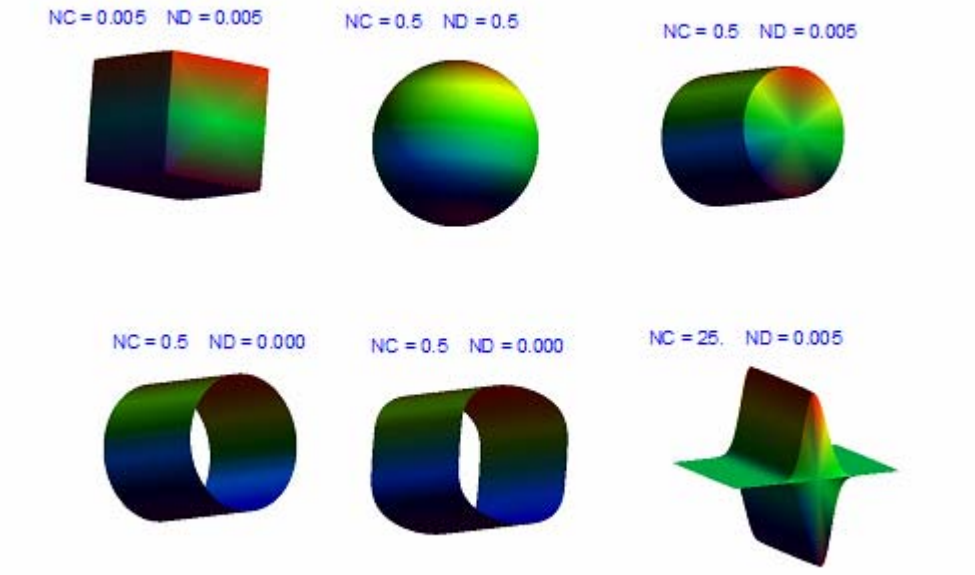

Figure 50. Geometries Derived As Class Function Distributions of Class Function Cross-Section Shapes

Fig. 51 shows the transformation of a thin square flat plate into a sphere. This is achieved by simultaneously increasing the cross-section and distribution exponents from 0.005 to 0.5 and at the same time increasing the length, L, from 0 to 1.

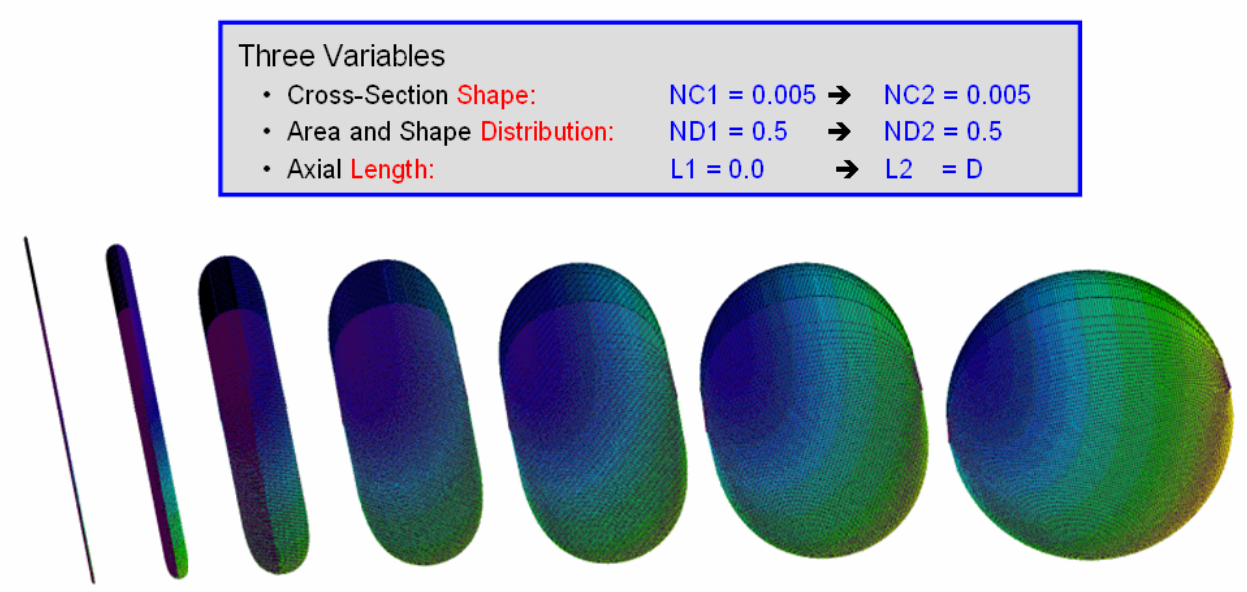

Figure 51. Transformation of a Flat Plate into a Sphere

Fig. 52 illustrates the transformation of a cube into an axi-symmetric Sears-Haack body, which as previously mentioned is the body shape for supersonic minimum wave drag. The cube transformation into a Sears-Haack body shown in the figure was achieved with three variables by simultaneous:

- Increasing the cross-section class function exponents from 0.005 to 0.75
- Increasing the longitudinal distribution function exponents from 0.005 to 0.5
- Increasing the length to keep the volume constant.

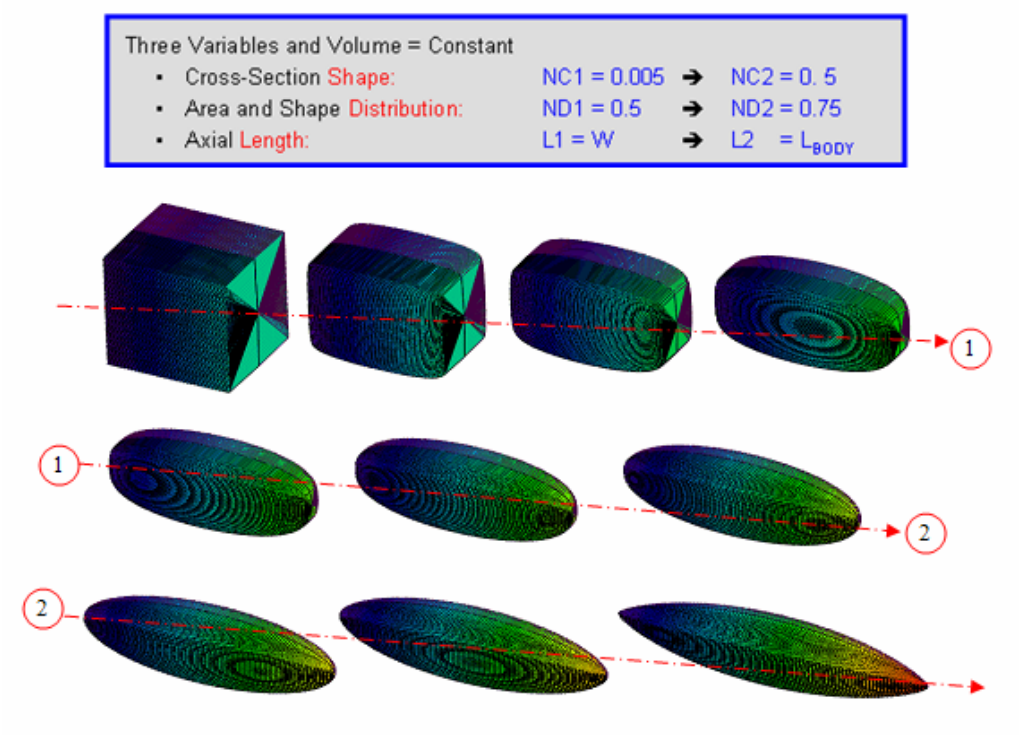

Figure 52. Three Variable Transformation of a Cube into a Sears-Haack Body

An example of transforming a constant area circular duct into a circular duct with geometry that varies from a circular inlet to a square shaped nozzle is shown in fig. 53.

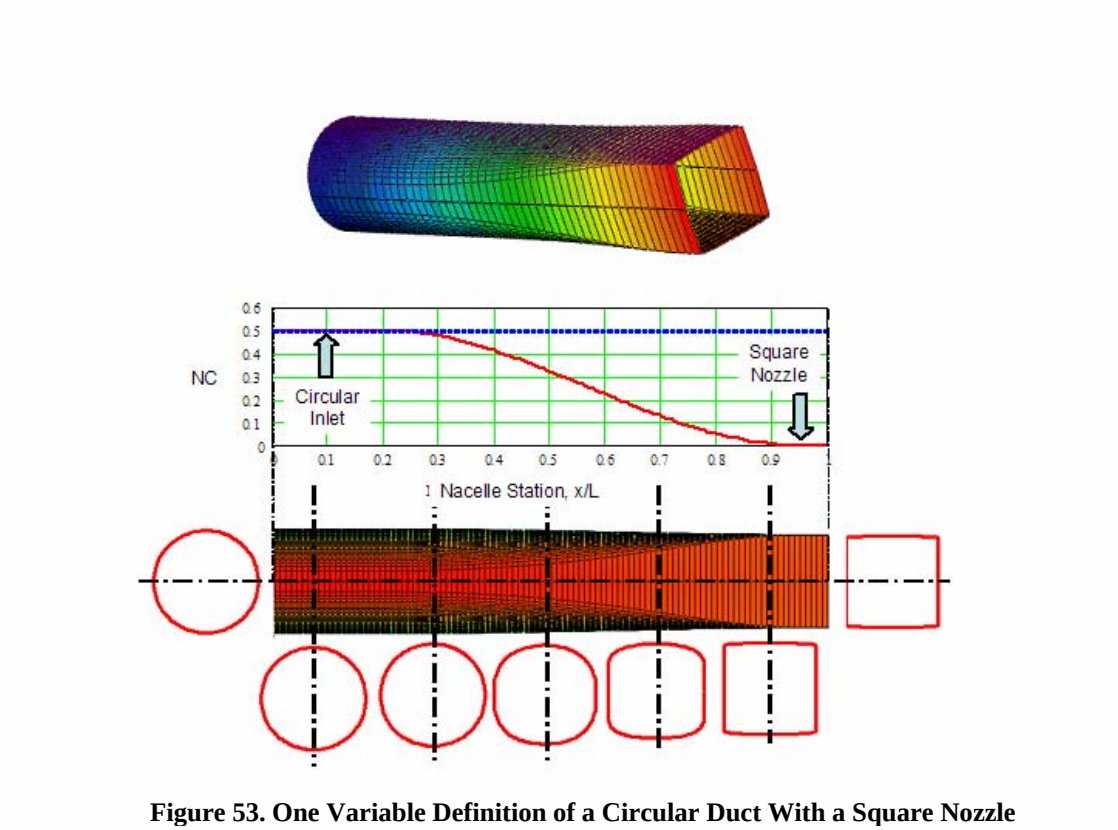

Figure 53. One Variable Definition of a Circular Duct With a Square Nozzle

In the previous example, the cross-section exponents are allowed to vary along the length. The initial geometry shape at the inlet is a circular duct defined with constant cross-section class function with exponents equal to 0.5. The duct geometry retains a constant cross section shape from 0 to 20% of the length. The last 5% of the length of the duct has a square cross-section which has class function exponents equal to 0.005. In between 20% and 95% of the length, the cross-section class function exponents were decreased from 0.5 at 20% to 0.001 at 95% by a cubic variation with zero slopes at both ends. Along the entire duct the width and depth were scaled proportionally to keep the cross section area constant. The distribution class function exponents equaled 0.0 to provide a flow through duct. The entire geometry is in reality driven by a single variable, the aft end constant class function exponent. This is an example of a "scalar loft" in which the geometry is generated by the variation of the shape parameters along the length of the duct using simple defining analytic equations.

The transformation of a circular duct into a thin wide rectangular duct is shown in the fig. 54.

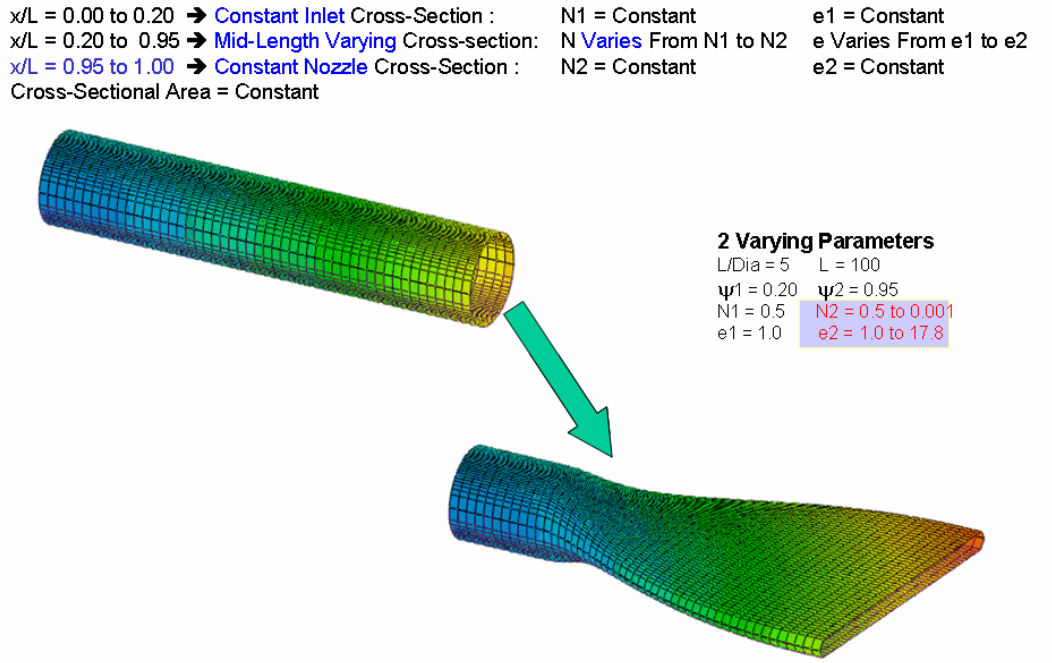

Figure 54. Transformation of a Circular Duct to a Thin Rectangular Nozzle ➔ 2 Variables

This transformation was derived from the previously example by the addition of a single additional variable, the nozzle aspect ratio. This is the ratio of the exit nozzle width the height. In this example, the additional variable varies from 1 to 17.8 as the cross-section class function exponent varies from 0.5 to 0.005.

In fig. 55, a circular duct is transformed into a supersonic aircraft configuration that resembles the Concorde, with a total of four design variables. The four design variables included:

- Distribution class function exponents: NDfwd, NDaft
- Aft end cross-section class function exponent, N2,
- the cross-section aspect ratio

A number of cross-section cuts through the final supersonic type configuration, are also shown in the figure.

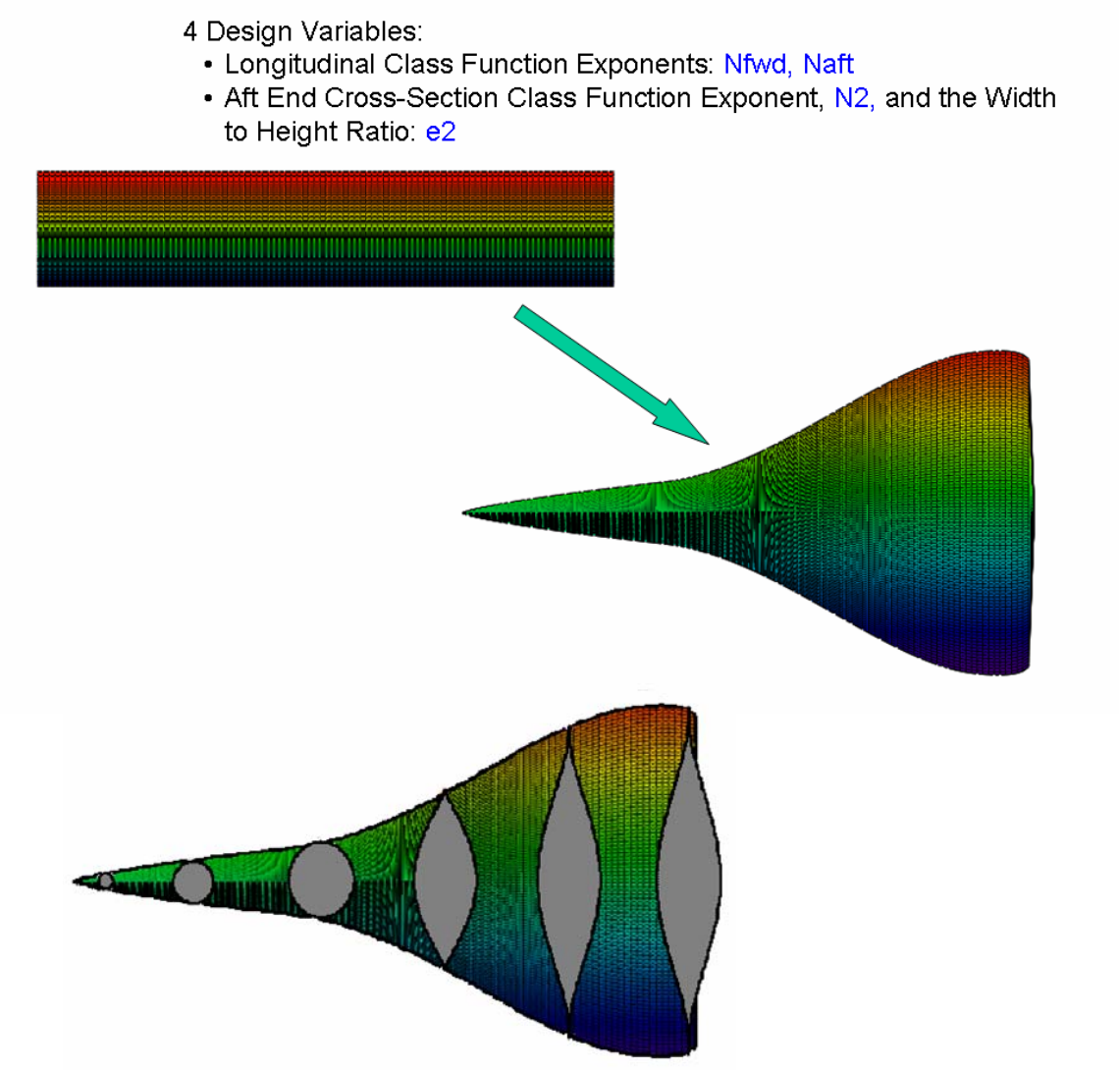

Figure 55. Circular Duct to Supersonic Wing-Body 3D Transformation ➔ 4 Variables

The concept of using the shape function / class function methodology to represent the cross-section shape and distribution of the cross-section shape together with the Bernstein polynomial representation of the shape functions has been subsequently extended to represent complete detailed wing / body /nacelle definitions in reference 13.

VII. Summary and Conclusions

- The analytic "Shape" Function plus "Class" function geometric transformation technique provides the capability to represent a wide variety of 2D and 3D geometries encompassing a very large design space with a relatively few scalar parameters.
- The "Class Function" / "Shape Function" airfoil representation methodology utilizing Bernstein polynomials has the following unique and very powerful properties:
  - Any smooth airfoil can be represented as "exactly" as desired.
  - This airfoil representation technique therefore, captures the entire design space of smooth and only smooth airfoils
  - Every airfoil in the entire design space can be derived from the unit shape function airfoil
  - Every airfoil can be derived from any other airfoil
  - Only a few terms of a Bernstein polynomial appear to be necessary to represent any airfoil geometry
  - Analytic Representation of Airfoils, Nacelles, Bodies, Wings with the ability to control leading edge radius, trailing edge boattail angle and ensure trailing edge closure
- The concept of using the shape function / class function methodology to represent both cross-section shape and the distribution of the cross-section shapes provides the capability to define a wide variety of 3D geometries wile requiring only a few design variables
- There are many potential uses for the analytic transformation methodology including:
  - Geometry smoothing and / or data enrichment
  - Computing surface derivatives
  - Geometry Extraction from drawings and figures
  - Airfoil Design Optimization
  - Nacelle Design Optimization
  - Wing Scalar Lofting
  - Wing Design optimization
  - PD optimization
  - Parametric trades and optimizations
  - Developing an understanding of key design variables

Appendix A

Bounding Values of the Shape Function for a Round Nose / Pointed Aft End Airfoil

A. Value of the Shape Function at the Trailing Edge

The general equation for a round nose airfoil with a sharp aft end was shown in this report is:

$$\xi(\psi) = \sqrt{\psi}\,(1-\psi)\,S(\psi) + \psi\,(\Delta\xi_{TE}) \tag{A1}$$

Non-dimensional airfoil station: $\psi = \frac{x}{C}$ ψ➔ 0 to 1

Non-dimensional airfoil ordinate: $\xi = \frac{z}{C}$

S(ψ) is the airfoil shape function:

Non-Dimensional upper surface trailing edge thickness ratio: $\Delta\xi = \frac{\Delta z_{TE}}{C}$

The airfoil slope can be calculated from eq.A1 using the chain rule of differentiation. The resulting equation is:

$$\xi'(\psi) = \sqrt{\psi}\,(1-\psi)\,S'(\psi) + \left[-\sqrt{\psi} + \frac{1}{2}(\psi)^{-1/2}(1-\psi)\right] S(\psi) + \Delta\xi_{TE} \tag{A2}$$

At the trailing edge, $\psi = 1$ and this equation becomes: $\zeta'(1) = -S(1) + \Delta\zeta_{TE}$ (A3)

The tangent of the boattail angle is defined as: $\tan(\beta) \equiv -\zeta'(1)$

Therefore: $S(1) = \tan(\beta) + \Delta\zeta_{TE}$ (A4)

Consequently the value of the shape factor at the trailing edge, $\psi = 1$, is equal to the tangent of the boattail angle plus the one half the non-dimensional half trailing edge thickness ratio.

B. Value of the Shape Function at the Leading Edge

In order to determine the value of the shape function at the leading edge, it is convenient to represent the shape function as a power series in the non-dimensional coefficient, ψ.

$$\xi(\psi) = \sqrt{\psi}\,(1-\psi)\sum_{i=0}^{\infty} A_i\psi^i + \psi\,(\Delta\xi_{TE}) \tag{A5}$$

Differentiating this equation, we obtain

$$\xi' = (1-\psi)\sum_{i=0}^{N}\left(i+1/2\right)A_i(\psi)^{i-1/2} - \sqrt{\psi}\sum_{i=0}^{N}A_i(\psi)^i + \Delta\xi_{TE} \tag{A6}$$

This can be rewritten as:

$$\zeta' = \sum_{i=0}^{N} A_i\left[\left(i+1/2\right)\psi^{i-1/2} - \left(i+3/2\right)\psi^{i+1/2}\right] + \Delta\xi_{TE} \tag{A7}$$

The second derivative can be obtained from the above equation.

$$\zeta'' = \sum_{i=0}^{N} A_i\left[\left(i+1/2\right)\left(i-1/2\right)\psi^{i-3/2} - \left(i+3/2\right)\left(i+1/2\right)\psi^{i-1/2}\right] \tag{A8}$$

The general equation for radius of curvature ρ(x) of the airfoil surface is:

$$\tilde{\rho}(\psi) = \frac{\left\{1+\left[\zeta'(\psi)\right]^2\right\}^{3/2}}{\zeta''(\psi)} \tag{A9}$$

Where $\tilde{\rho}(x) = \dfrac{\rho(x)}{C}$

Substituting equations A7 and A8 into A9 we obtain:

$$\tilde{\rho}(\psi) = \frac{\left\{1+\left\{\sum_{i=o}^{N} A_i\left[\left(i+1/2\right)\psi^{i-1/2} - \left(i+3/2\right)\psi^{i+1/2}\right] + \Delta\zeta\right\}^2\right\}^{3/2}}{\sum_{i=0}^{N} A_i\left[\left(i+1/2\right)\left(i-1/2\right)\psi^{i-3/2} - \left(i+3/2\right)\left(i+1/2\right)\psi^{i-1/2}\right]} \tag{A10}$$

In order to develop the expression for the radius of curvature at the airfoil nose, extract the dominant terms from both the numerator and denominator in equation A10. These are the first terms in both equations. Equation A10 then becomes

$$\tilde{\rho}(\psi) = \frac{\left\{1+\left\{\frac{A_0}{2}\psi^{-1/2} - \frac{3A_0}{2}\psi^{1/2} + \sum_{i=1}^{N} A_i\left[\left(i+1/2\right)\psi^{i-1/2} - \left(i+3/2\right)\psi^{i+1/2}\right] + \Delta\zeta\right\}^2\right\}^{3/2}}{-\frac{A_0}{4}\psi^{-3/2} - \frac{3A_0}{4}\psi^{-1/2} + \sum_{i=1}^{N} A_i\left[\left(i+1/2\right)\left(i-1/2\right)\psi^{i-3/2} - \left(i+3/2\right)\left(i+1/2\right)\psi^{i-1/2}\right]} \tag{A11}$$

This can be rearranged as:

$$\tilde{\rho}(\psi) = \frac{\left\{1+\frac{A_0^2}{4}\psi^{-1}\left\{1-3\psi+\frac{2}{A_0}\sum_{i=1}^{N} A_i\left[\left(i+1/2\right)\psi^{i} - \left(i+3/2\right)\psi^{i+1}\right] + \frac{2}{A_0}\psi^{1/2}\Delta\zeta\right\}^2\right\}^{3/2}}{-\frac{A_0}{4}\psi^{-3/2}\left\{1+3\psi-\frac{4}{A_0}\sum_{i=1}^{N} A_i\left[\left(i+1/2\right)\left(i-1/2\right)\psi^{i} - \left(i+3/2\right)\left(i+1/2\right)\psi^{i+1}\right]\right\}} \tag{A12}$$

And by further arrangement, the equation becomes:

$$\tilde{\rho}(\psi) = \frac{\left[\left(\frac{A_0}{2}\right)^2\psi^{-1}\right]^{3/2}\left\{\frac{2}{A_0}\psi+\left\{1-3\psi+\frac{2}{A_0}\sum_{i=1}^{N} A_i\left[\left(i+1/2\right)\psi^{i} - \left(i+3/2\right)\psi^{i+1}\right] + \frac{2}{A_0}\psi^{1/2}\Delta\zeta\right\}^2\right\}^{3/2}}{-\frac{A_0}{4}\psi^{-3/2}\left\{1+3\psi-\frac{4}{A_0}\sum_{i=1}^{N} A_i\left[\left(i+1/2\right)\left(i-1/2\right)\psi^{i} - \left(i+3/2\right)\left(i+1/2\right)\psi^{i+1}\right]\right\}} \tag{A13}$$

As ψ ➔0, the terms in the brackets { } ➔ 1

$$\tilde{\rho}(\psi) = -\frac{R_{LE}}{C} = \frac{\left[\left(\frac{A_0}{2}\right)^2\psi^{-1}\right]^{3/2}}{-\frac{A_0}{4}\psi^{-3/2}} = \frac{-A_0^2}{2} \tag{14}$$

This becomes:

$$A_0 = \sqrt{2\frac{R_{LE}}{L}} \tag{15}$$

Therefore, the value of the shape function at the leading edge is directly related to the leading edge radius of curvature.

References

[1] Helmut Sobieczky, H., "Aerodynamic Design and Optimization Tools Accelerated by Parametric Geometry Preprocessing", European Congress on Computational Methods in Applied Sciences and Engineering, ECCOMAS 2000, 11-14 September 2000

[2] Sobieczky, H., "Parametric Airfoils and Wings, "Notes on Numerical Fluid Mechanics", Vol. 68, pp.71-88, Vieweg Verlag, 1998

[3] Samareh, J.A., "Survey of Shape Parameterization Techniques for High-Fidelity Multidisciplinary Shape Optimization", AIAA JOURNAL Vol. 39, No. 5, May 2001

[4] Robinson, G. M., and Keane, A. J., "Concise Orthogonal Representation of Supercritical Airfoils", Journal of Aircraft, Vol. 38, NO. 3

[5] Song, W., and Keane, A.J., "A Study of Shape Parameterisation Airfoil Optimisation", AIAA-2004-4482
10th AIAA/ISSMO Multidisciplinary Analysis and Optimization Conference, Albany, New York, Aug. 30-1, 2004

[6] Padula, S., and Li, W., "Options for Robust Airfoil Optimization Under Uncertainty", 9th AIAA Multidisciplinary Analysis and Optimization Symposium, 4-6 September 2002

[7] Hicks, R. M. and Henne, P. A.,"Wing design by numerical optimization", Journal of Aircraft, Vol. 15, pp. 407-412, 1978.

[8] Padula, S., and Li, W., "Options for Robust Airfoil Optimization Under Uncertainty", 9th AIAA Multidisciplinary Analysis and Optimization Symposium, 4-6 September 2002

[9] Timothy W. Purcell, T. W., and Om, D., "TRANAIR Packaging for Ease-of-Use in Wing Design", AIAA-1998-5575, AIAA and SAE, 1998 World Aviation Conference, Anaheim, CA, Sept. 28-30, 1998

[10] Smith, M. W., "User-friendly CFD - Application to TRANAIR for Analysis of Transport Aircraft", AIAA-1998-5574, AIAA and SAE, 1998 World Aviation Conference, Anaheim, CA, Sept. 28-30, 1998

[11] Samant, S. S., Bussoletti, J. E., Johnson, F. T., Burkhart, R. H., Everson, B. L., Melvin, R. G., Young, D. P., Erickson, L. L., and Madson, M. D., "TRANAIR - A Computer Code for Transonic Analyses of Arbitrary Configurations", AIAA-1987-34, Aerospace Sciences Meeting, 25th, Reno, NV, Jan 12-15, 1987

[12] Cenko, A., Tseng, W., Phillips, K., and Madson, M., "TranAir Applications to Transonic Flowfield Predictions", AIAA-1991-201, Aerospace Sciences Meeting, 29th, Reno, NV, Jan 7-10, 1991.

[13] Kulfan, B. M., "Universal Parametric Geometry Representation Method – CST", 45th AIAA Aerospace Sciences Meeting and Exhibit, 8 - 11 January 2007